The Influence of Wind Effects upon Internal Tides in Shelf Edge Regions

JIUXING XING AND ALAN M. DAVIES

Proudman Oceanographic Laboratory, Bidston Observatory, Birkenhead, Merseyside, United Kingdom

(Manuscript received 23 October 1995, in final form 21 June 1996)

ABSTRACT

The interaction of the internal tide with wind-induced currents in the shelf edge region off the west coast of Scotland is studied using a baroclinic shelf edge model. The model is used in cross-shelf form with a horizontal finite-difference grid of the order of 0.6 km and 50 sigma levels in the vertical to study the modification of the internal tide produced by upwelling and downwelling winds. Horizontal mixing in the model is parameterized using either the Laplacian form of the horizontal diffusion or the biharmonic form and the sensitivity of the solution to both forms is examined.

Coefficients for the vertical diffusion of momentum and density are determined using either an algebraic expression involving the Richardson number or from a two-equation turbulence energy submodel.

Calculations show that in the case of an upwelling-favorable wind the density gradient in the near-bed region is increased leading to a slight modification (compared to the tide only solution) of the internal tide at the fundamental frequency with significant increases in amplitude of the higher harmonics due to the increase in the nonlinear terms produced by the increase in the density gradient. With a downwelling-favorable wind the amplitude of the current and internal displacement of the internal tide at the fundamental frequency are significantly reduced due to the change in the density field in the region of internal tidal production. This also leads to a reduction in the amplitude of the higher tidal harmonics.

By using a fine grid in the horizontal, the coefficients in the horizontal diffusion terms were set at a minimum and no significant difference in solutions computed with the Laplacian or biharmonic diffusion terms was found. Similarly there are no differences in the major features of the flow field computed with the various parameterizations of the vertical diffusion, although there are some differences in the magnitude of the diffusion coefficients.

1. Introduction

Although significant progress has been made in identifying the mechanisms influencing the production and propagation of internal tides in shelf edge regions (Craig 1987; Baines 1982; Sherwin 1988, 1991), little has been done to examine the influence of other effects such as wind events upon them.

It is well known that in shallow water the nonlinear coupling between tidal and wind-driven flows during major storm events modifies surge elevations (tide–surge interaction) (Proctor and Wolf 1990). Also, in a recent series of papers (Davies and Lawrence 1994, 1995; Signel et al. 1990), it has been shown that enhanced turbulence due to wind-driven flows, and in shallow water the wind wave orbital velocity at the seabed can modify both the tidal elevations and currents.

In the shelf edge region off the west coast of Scotland where the stratification intersects the slope and the barotropic tide has a significant amplitude (Xing and Davies 1996a; Proctor and Davies 1996), a large internal tide can be generated (Sherwin 1988, 1991; Sherwin and Taylor 1989, 1990). In general, the majority of models that have been used to study the internal tide have been semianalytical and dealt with the linear inviscid solution (Baines 1982; Craig 1987; New and Pingree 1990; New 1988) and in many cases have been restricted to idealized topography and density. However, recently a full three-dimensional model that can take account of realistic bottom topography and density has been used by Holloway (1996) to study the internal tide. Also Sherwin and Taylor (1990) used the finite-difference model of Chuang and Wang (1981) to examine the role

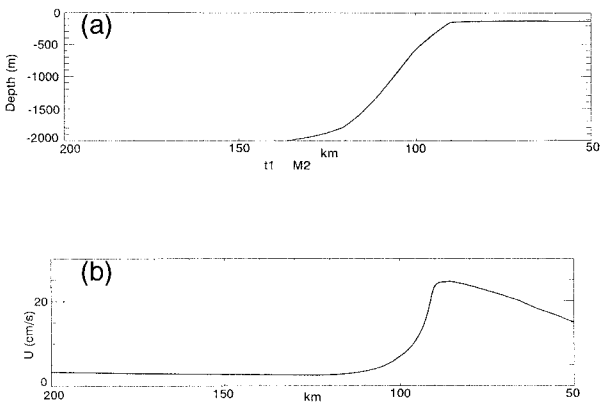

FIG. 1. Cross-section variation of (a) water depths (m) and (b) barotropic M_2 tidal current.

Corresponding author address: Dr. Alan M. Davies, Proudman Oceanographic Laboratory, Bidston Observatory, Birkenhead, Merseyside L43 7RA, United Kingdom.

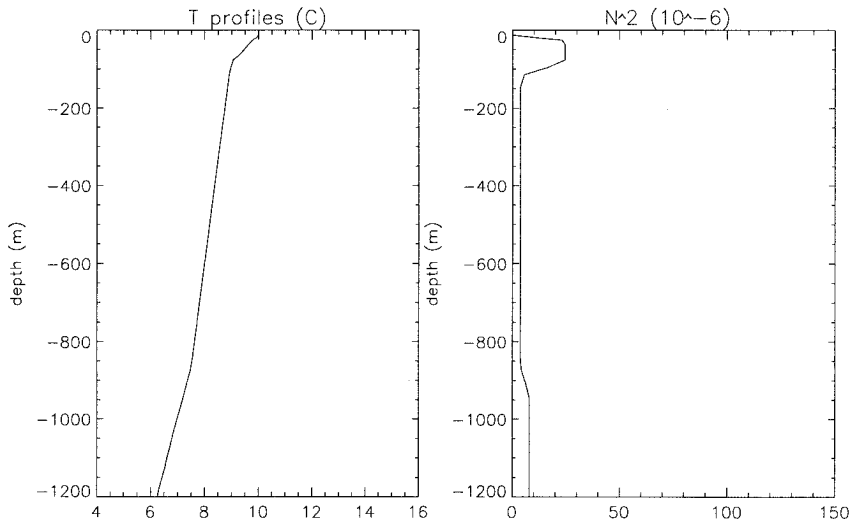

FIG. 2. Profiles of temperature T(°C) and Brunt–Väisällä frequency $N^2 \times 10^{-6}$ (s^{-1}) for winter.

of density and topography upon internal tides. Although this model can accommodate an arbitrary cross-sectional variation in density and topography, it is restricted to the linear equations. Also, time dependency was removed by considering a single harmonic, and vertical eddy viscosity was neglected although some linear damping was included.

In this paper we use a three-dimensional nonlinear baroclinic primitive equation model to examine how the internal tide at the shelf edge off the west coast of Scotland is modified by upwelling- and downwelling-favorable winds. The model uses a number of methods to parameterize the internal mixing, from a simple Richardson number–dependency (Munk and Anderson 1948) up to the application of a two-prognostic-equation turbulence energy model (Blumberg and Mellor 1987). By this means, the sensitivity of the mixing to the parameterization of subgrid-scale processes is examined. Also, since the internal tides are particularly sensitive to the gradient of the density field, then besides the influence of the parameterization of turbulence upon mixing processes, it will have a significant influence upon the internal tide in the shelf edge region. This effect will probably be larger at the shelf edge than in a shallow water region.

The hydrodynamic equations and turbulence models are presented in the next section, with subsequent sections dealing with the results of the numerical calculations and conclusions.

TABLE 1. Summary of tidal and wind stress forcing and parameterization of subgrid-scale turbulence used in the model.

Calcn.	Tide	Wind condition	Subgrid parameterization
1	yes	no	$q^2 - q^2l$
2	no	upwelling	$q^2 - q^2l$
3	no	downwelling	$q^2 - q^2l$
4	yes	upwelling	$q^2 - q^2l$
5	yes	downwelling	$q^2 - q^2l$
6	yes	upwelling	algebraic
7	yes	downwelling	algebraic

2. The three-dimensional baroclinic model

a. Hydrodynamic equations

A three-dimensional, free-surface, primitive equation model is used in the calculations. The equations in transport form in σ coordinates where $\sigma = (\zeta + z)/H$ are given by

$$\frac{\partial Hu}{\partial t} + \nabla(Hu\mathbf{V}) + \frac{\partial Hu\omega}{\partial \sigma} - fHv = -gH\frac{\partial \zeta}{\partial x} + \mathrm{BPF}_x + \frac{1\partial}{H^2\partial\sigma}\left(K_m\frac{\partial Hu}{\partial \sigma}\right) + HF_u, \tag{1}$$

$$\frac{\partial Hv}{\partial t} + \nabla(Hv\mathbf{V}) + \frac{\partial Hv\omega}{\partial \sigma} + fHu = -gH\frac{\partial \zeta}{\partial y} + \mathrm{BPF}_y + \frac{1\partial}{H^2\partial\sigma}\left(K_m\frac{\partial Hv}{\partial \sigma}\right) + HF_v, \tag{2}$$

$$\frac{\partial \zeta}{\partial t} + \nabla\left(\int_{-1}^{0} (H\mathbf{V})\, d\sigma\right) = 0, \tag{3}$$

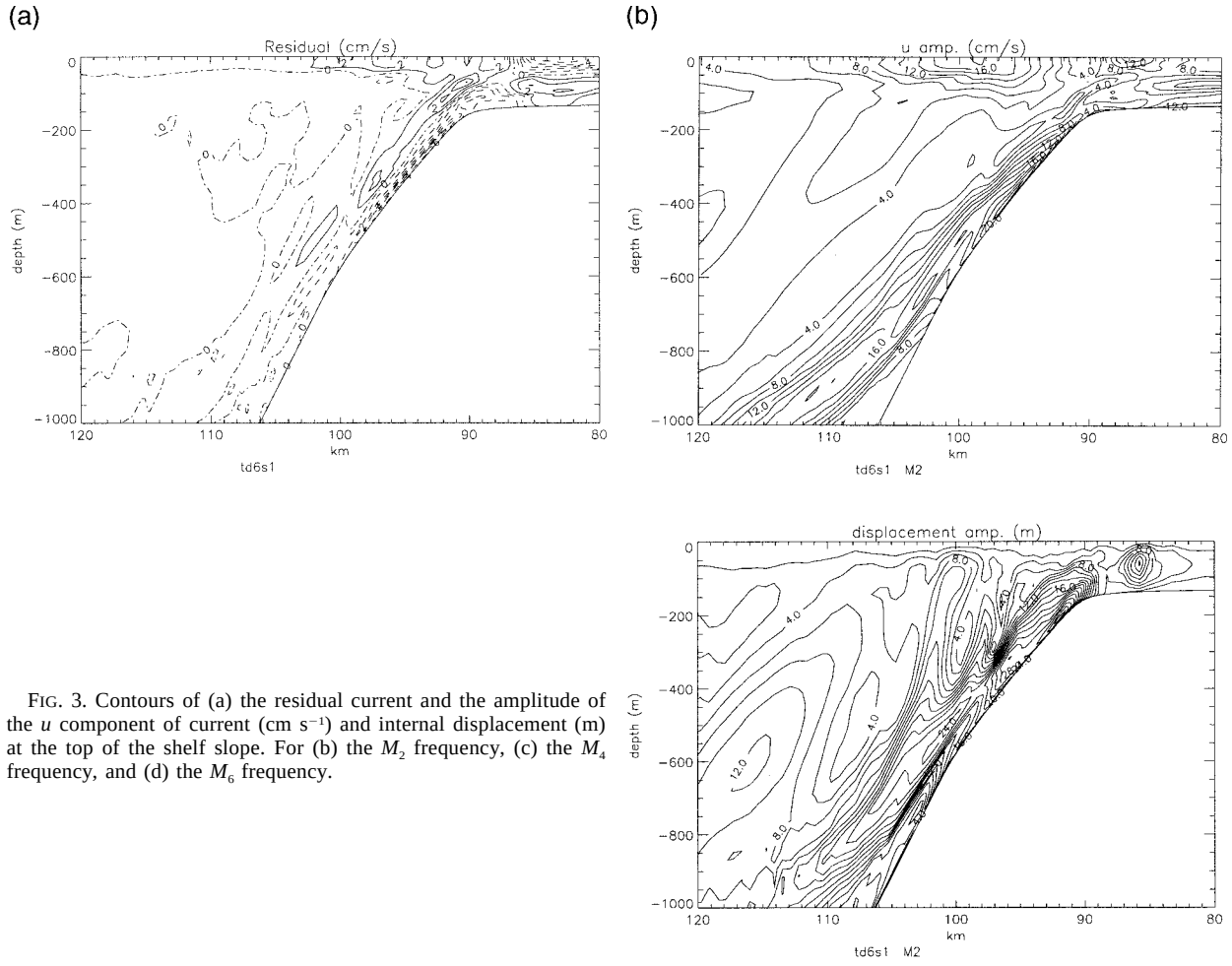

FIG. 3. Contours of (a) the residual current and the amplitude of the u component of current (cm s^{-1}) and internal displacement (m) at the top of the shelf slope. For (b) the M_2 frequency, (c) the M_4 frequency, and (d) the M_6 frequency.

$$\frac{\partial HT}{\partial t} + \nabla(HT\mathbf{V}) + \frac{\partial HT\omega}{\partial \sigma} = \frac{1}{H^2}\frac{\partial}{\partial \sigma}\left(K_h\frac{\partial HT}{\partial \sigma}\right) + HF_T, \tag{4}$$

$$\frac{\partial P}{\partial \sigma} = -\rho g H, \tag{5}$$

with density computed from temperature using

$$\rho = \rho_0[1 - \alpha(T - T_0)]. \tag{6}$$

In these equations, $V = (u, v)$ and (u, v, ω) are the velocity components corresponding to the (x, y, σ) coordinates; ρ is the density; T is the temperature; α is the thermal expansion coefficient: T_0 and ρ_0 are the reference temperature and density respectively; H is the total water depth; ζ is the elevation of the sea surface above the undisturbed level; z is the water depth increasing vertically upward with $z = \zeta$ the free surface and $z = -h$ the seabed; f is the Coriolis parameter; g is the gravitational acceleration; t is time; K_m and K_h are vertical eddy viscosity and diffusivity coefficents; F_u, F_v, and F_T are horizontal diffusions for the momentum and temperature; P is the pressure field. In these equations the baroclinic pressure force terms (BPF_x, BPF_y) are given by

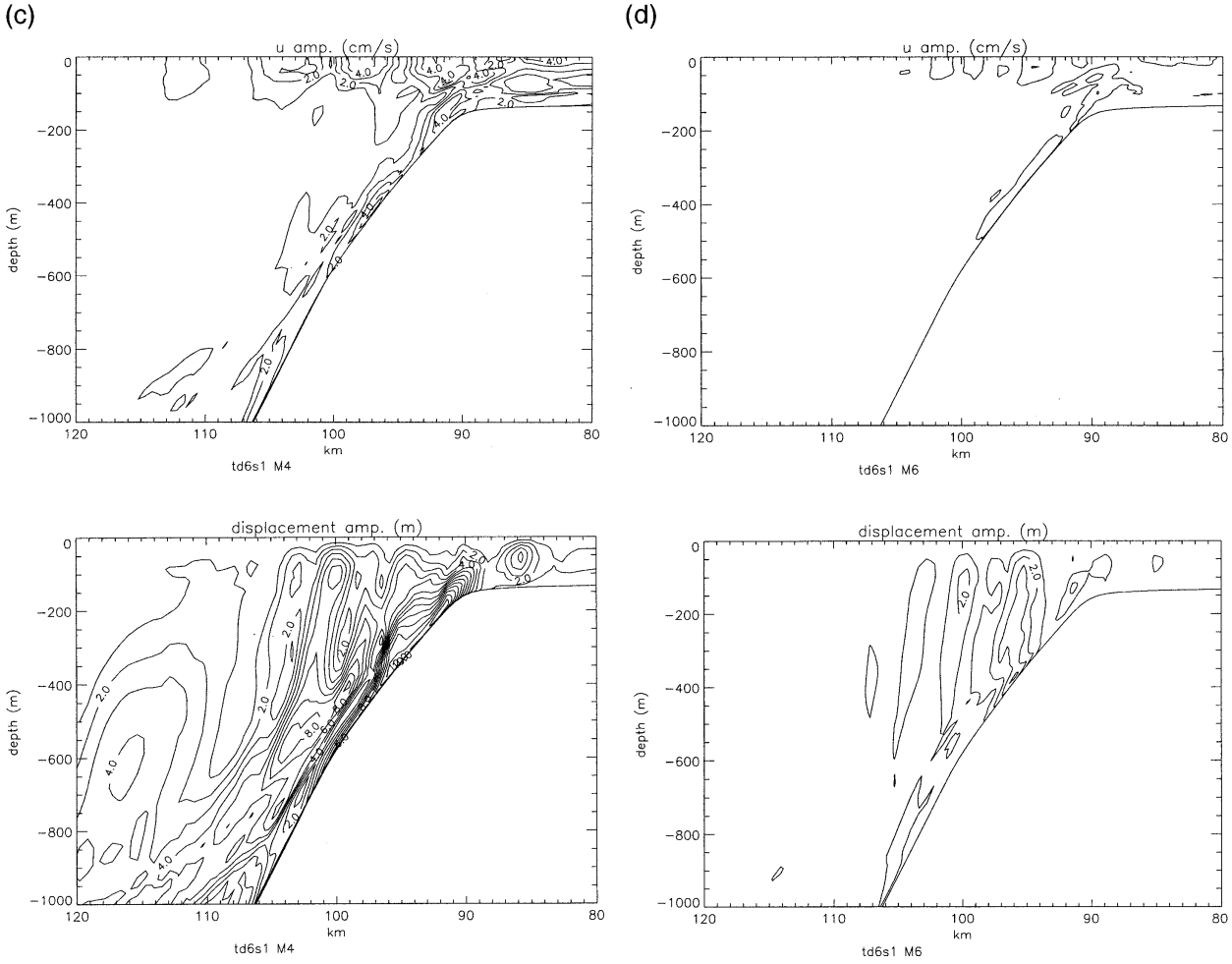

FIG. 3. (*Continued*)

$$\mathrm{BPF}_x = -\frac{H\partial P_{b_0}}{\rho\partial x}\bigg|_z - \frac{H}{\rho_0}\left(\frac{\partial(P_b - P_{b_0})}{\partial x} + \frac{\sigma}{H}\frac{\partial(P_b - P_{b_0})}{\partial\sigma}\frac{\partial H}{\partial x} + \frac{\partial(P_b - P_{b_0})}{H\partial\sigma}\frac{\partial\zeta}{\partial x}\right) \tag{7}$$

$$\mathrm{BPF}_y = -\frac{H\partial P_{b_0}}{\rho\partial y}\bigg|_z - \frac{H}{\rho_0}\left(\frac{\partial(P_b - P_{b_0})}{\partial y} + \frac{\sigma}{H}\frac{\partial(P_b - P_{b_0})}{\partial\sigma}\frac{\partial H}{\partial y} + \frac{\partial(P_b - P_{b_0})}{H\partial\sigma}\frac{\partial\zeta}{\partial y}\right), \tag{8}$$

where P_{b_0} is a reference baroclinic pressure or the initial baroclinic pressure field. The first terms on the right-hand side of Eqs. (7) and (8) are the pressure forces calculated in z coordinate, and thus only deviations of the pressure forces are calculated in the σ coordinate. In this way errors due to the coordinate transformation can be reduced. The horizontal diffusion terms F_u, F_v, and F_T in Eqs. (1), (2), and (4) are parameterized in terms of either a Laplacian or a biharmonic horizontal viscous term (Heathershaw et al. 1994).

These equations involve use of the hydrostatic assumption, which is commonly used (e.g., Baines 1982; Craig 1987; New 1988; Sherwin 1988; Holloway 1996) in studying internal tides at the shelf edge, although recently Lamb (1994) used a nonhydrostatic model. For the calculations considered here, which are primarily concerned with the influence of wind effects upon internal tides, this assumption is valid.

A time-splitting method is used to integrate the hydrodynamic equations in order to reduce the computational time. This is accomplished by writing u and v as

$$u = U + u', \qquad v = V + v',$$

where U and V are the depth-mean horizontal velocity (external mode) and u' and v' are the depth-dependent horizontal velocity (internal mode). Since the external

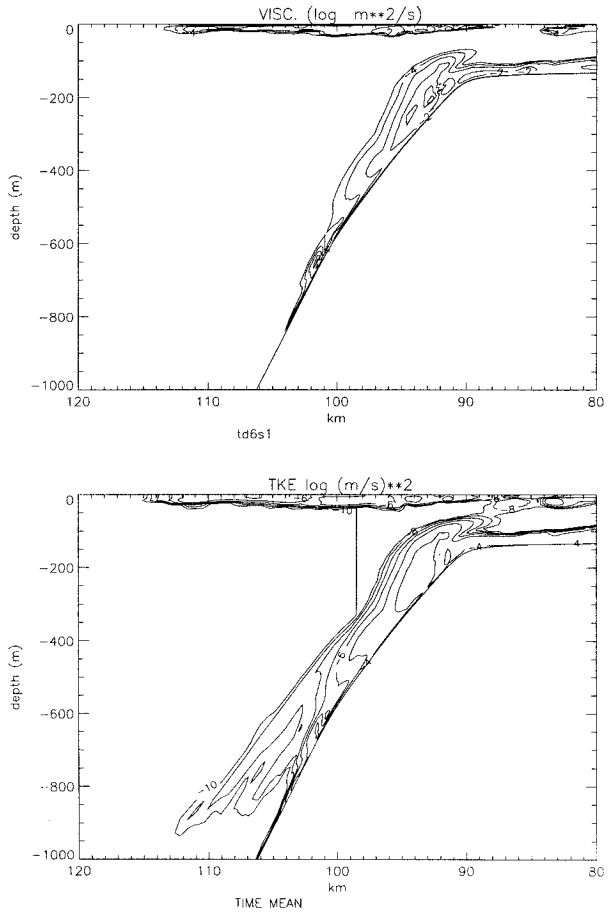

FIG. 4. Contours of the time averaged over an M_2 period of (a) $\log_{10}$ of vertical eddy viscosity ($m^2\ s^{-1}$) and (b) $\log_{10}$ of turbulence energy ($m^2\ s^{-2}$).

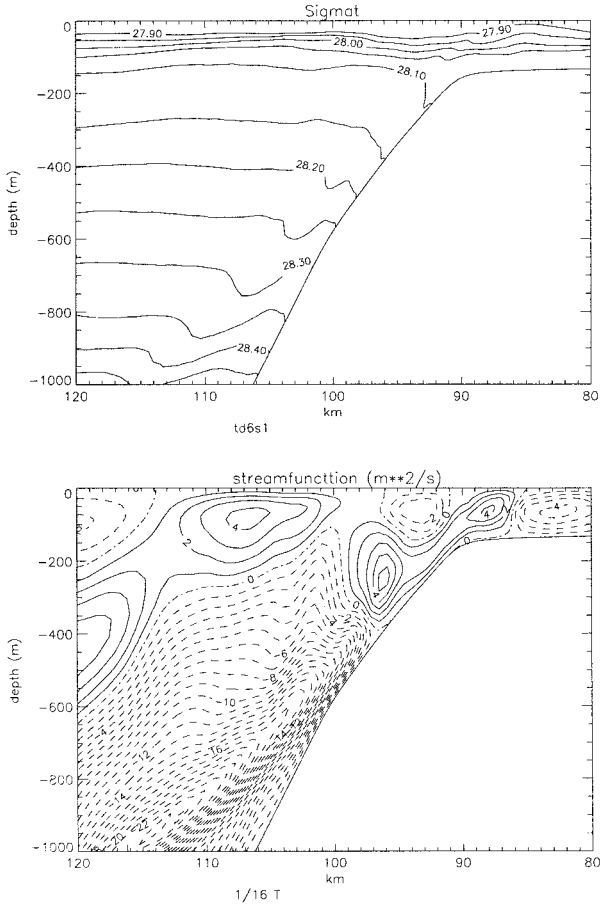

FIG. 5. Contours over an M_2 tidal cycle T of sigma-t (σ_t) and the streamfunction at the top of the shelf slope. (Solid is a positive value, with dashed a negative value, and dotted and dashed the zero contour).

mode represents the fast-moving gravity waves, a small time step is required for the time integration of the free surface wave, which involves U and V in order to satisfy the CFL condition. The internal mode, however, represents slow-moving waves and hence much larger time steps can be used. To avoid errors in the mass conservation due to use of the time-splitting method, the sea surface elevation is recomputed before the internal mode equations are integrated by using the depth-mean velocity of the time mean in the smaller time step. The vertical velocity ω, therefore, is calculated from

$$\frac{\partial Hu'}{\partial x} + \frac{\partial Hv'}{\partial y} + \frac{\partial H\omega}{\partial \sigma} = 0. \tag{9}$$

The time-splitting approach is a numerical method of reducing computer time and does not depend upon any assumption concerning the mechanisms, namely internal viscous effects, or baroclinic forcing that produce changes in current through the vertical. The role of viscosity and internal pressure gradients in determining tidal current profiles is discussed later.

Discretization in the horizontal is accomplished using a staggered Arakawa-C finite-difference grid. In the vertical a standard finite-difference grid on a sigma coordinate is applied. The vertical diffusion terms, computed using a range of turbulence energy models, are computed by a fully implicit scheme. Details of the numerical method have been presented elsewhere (Davies and Jones 1990, 1991; Xing and Davies 1996a,b,c; Davies and Xing 1995) and will not be repeated here.

b. Formulation of vertical viscosity and diffusivity

The determination of the vertical eddy viscosity and diffusivity in the model is either in terms of turbulence energy and mixing length, both of which are computed from a turbulence energy model (see below), or as an algebraic expression in which they are related to the Richardson number (see later discussion)

1) TURBULENCE ENERGY MODEL

A well-established turbulence energy model (Blumberg and Mellor 1987) that has been widely used in ocean modeling (Oey and Chen 1992a,b) involves prognositic

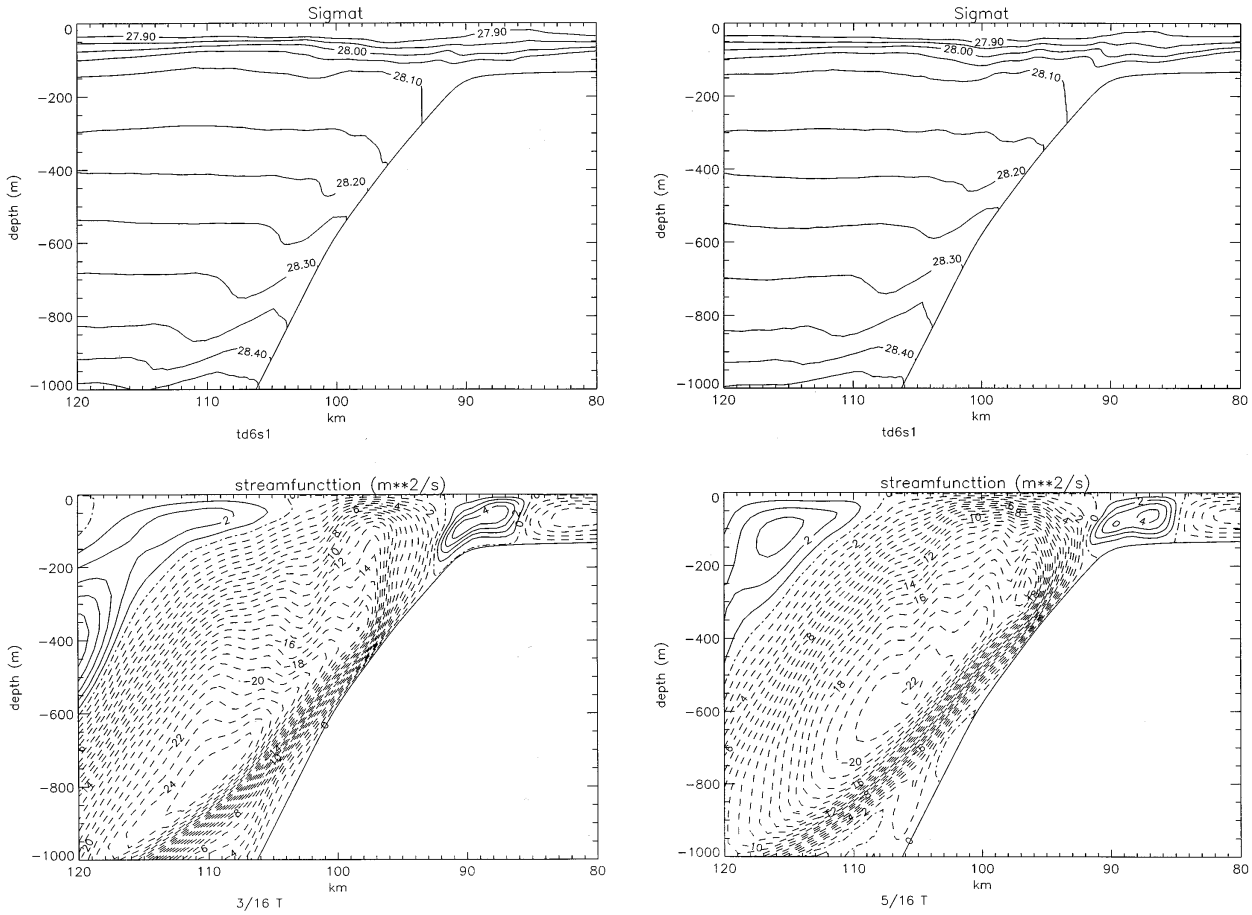

FIG. 5. (*Continued*)

equations for the turbulence energy and mixing length [known as the q^2–q^2l model, where $q^2 = 2E$, with E turbulence kinetic energy (TKE), and l the mixing length], in sigma coordinates is given by

$$\frac{\partial q^2 H}{\partial t} + \nabla\cdot(Hq^2\mathbf{V}) + \frac{\partial Hq^2\omega}{\partial\sigma} = 2\frac{K_m}{H}\left[\left(\frac{\partial u}{\partial\sigma}\right)^2 + \left(\frac{\partial v}{\partial\sigma}\right)^2\right] + \frac{2gK_h}{\rho}\frac{\partial\rho}{\partial\sigma} - \frac{2q^3H}{B_1 l} + \frac{1}{H^2}\frac{\partial}{\partial\sigma}\left(S_q q l\frac{\partial q^2 H}{\partial\sigma}\right) + HF_q \tag{10}$$

and

$$\frac{\partial q^2 lH}{\partial t} + \nabla\cdot(Hq^2 l\mathbf{V}) + \frac{\partial Hq^2 l\omega}{\partial\sigma} = \frac{lE_1K_m}{H}\left[\left(\frac{\partial u}{\partial\sigma}\right)^2 + \left(\frac{\partial v}{\partial\sigma}\right)^2\right] + \frac{lE_1gK_h}{\rho_0}\frac{\partial\rho}{\partial\sigma} - \frac{q^3}{B_1}WH + \frac{1}{H}\frac{\partial}{\partial\sigma}\left(S_q q l\frac{\partial q^2 l}{\partial\sigma}\right) + HF_l. \tag{11}$$

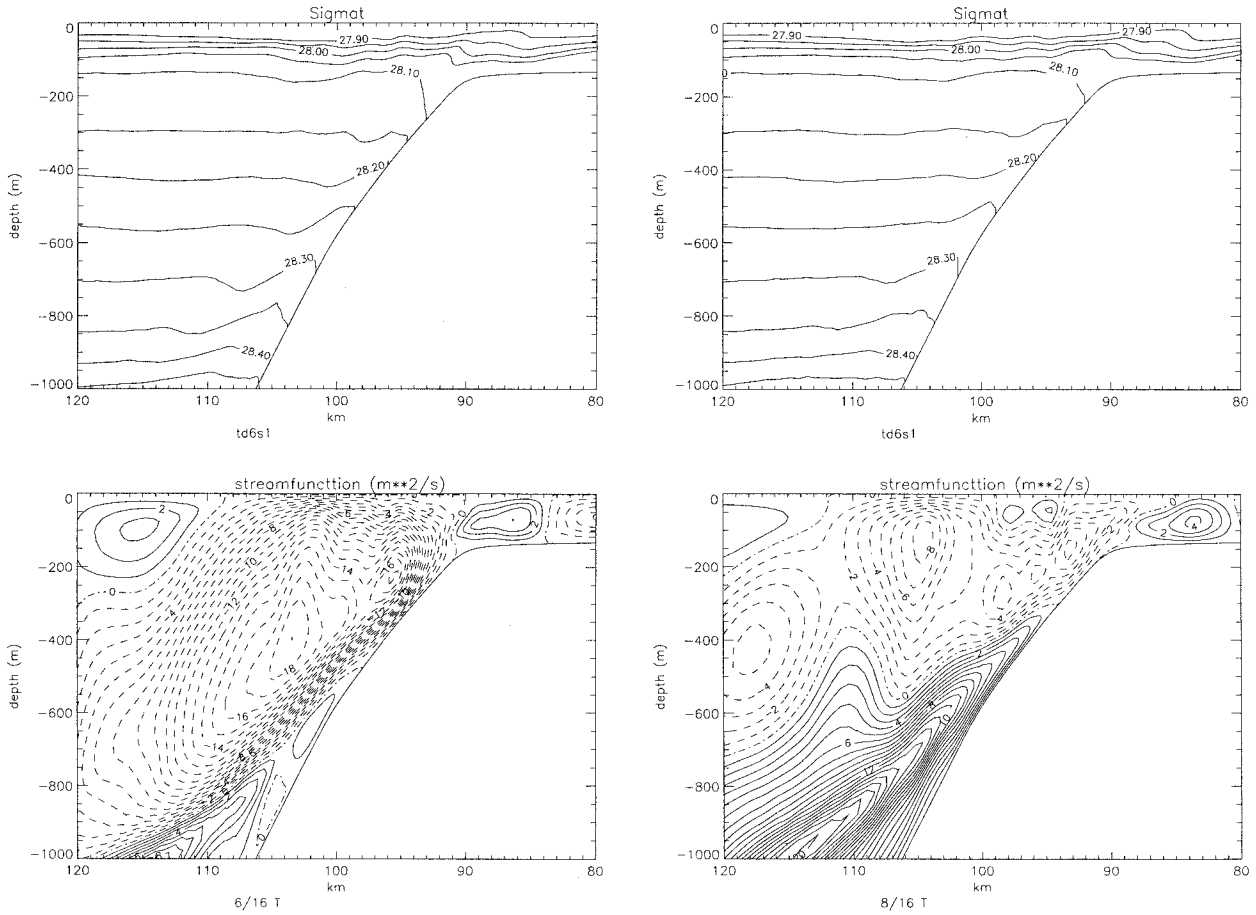

FIG. 5. (*Continued*)

In these equations, W is a wall proximity function, which is defined by

$$W = 1 + E_2\left(\frac{l}{\kappa L}\right)^2, \tag{12}$$

with L given by

$$(L)^{-1} = (\zeta - z)^{-1} + (H + z)^{-1} \tag{13}$$

and $\kappa = 0.4$ is von Kármán's constant.

The eddy viscosity and eddy diffusivity are computed from

$$K_m = lqS_M, \qquad K_h = lqS_H \tag{14}$$

with S_M and S_H the stability functions, the form of which are given by Galperin et al. (1988, 1989) and will not be repeated here.

In these equations, the coefficients are given by $A_1 = 0.92$, $A_2 = 0.74$, $B_2 = 10.1$, $C_1 = 0.08$, $S_q = 0.2$, $B_1 = 16.6$, and $E_1 = 1.33$. Following Galperin et al. (1989), a limiting condition is applied to the length scale of the form,

$$l \leq \frac{k_l q}{N^2}, \tag{15}$$

where k_1 is a constant determined from laboratory and observational data and N^2 the buoyancy frequency. The importance of limiting the mixing length using Eq. (15) and its influence upon the solutions is discussed in Gaspar et al. (1990) and Luyten (1996).

The q^2–q^2l turbulence energy model is not the only turbulence model available in the literature (Johns and Oguz 1987), and the k–ϵ model has been used in tidal simulations (Baumert and Radach 1992). Also a comparison of the various models is presented in Luyten et al. (1996). Some problems with the k–ϵ model were found by Davies and Gerritsen (1994) in studying tides in the Irish Sea, whereas Xing and Davies (1996b,c) found that when using the q^2–q^2l model the tidal currents could be accurately determined in the region. For this reason the q^2–q^2l model is used here in preference to the k–ϵ model.

2) ALGEBRAIC EDDY VISCOSITY AND DIFFUSIVITY

In addition to the turbulence model, calculations were performed using a simple Richardson-number-dependent eddy viscosity and eddy diffusivity formulation.

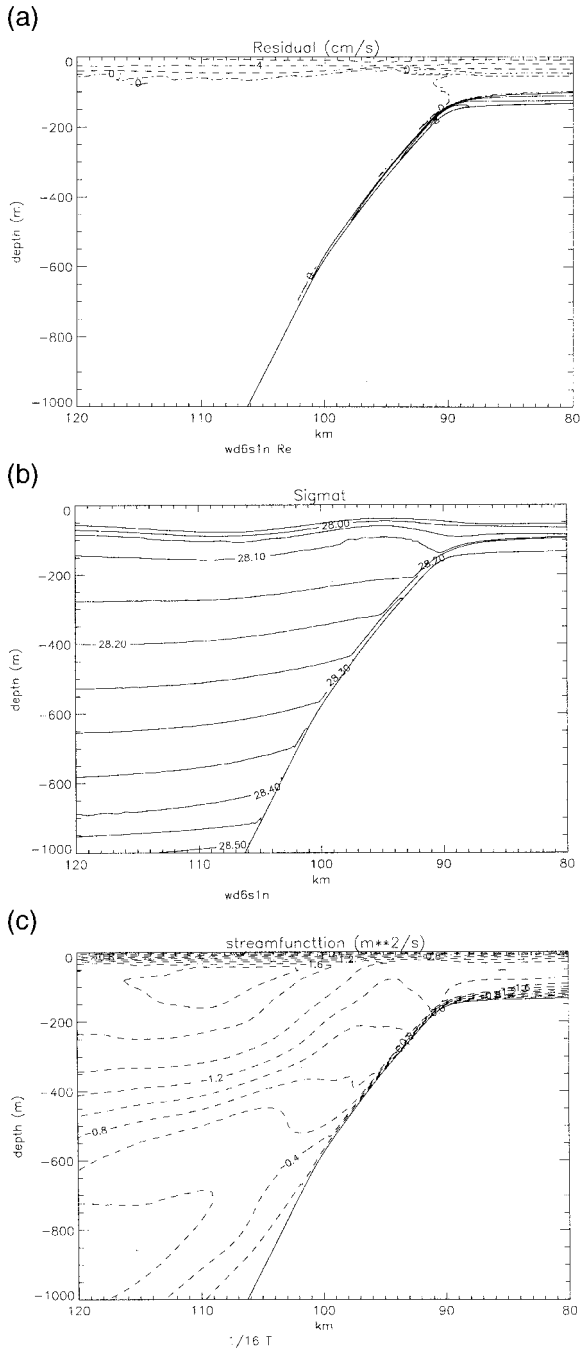

FIG. 6. Contours of (a) the u component of current (cm s^{-1}), (b) the sigma-t (σ_t) surfaces, and (c) streamfunction contours produced by an upwelling wind stress condition having a magnitude of 0.2 N m^{-2}. (Solid contour is a positive value, with dashed a negative value).

Following Munk and Anderson (1948), the eddy viscosity and eddy diffusivity take the form

$$K_m = A_{r1}\psi_1 + B_{r1} \tag{16}$$

$$K_h = A_{r2}\psi_2 + B_{r2}, \tag{17}$$

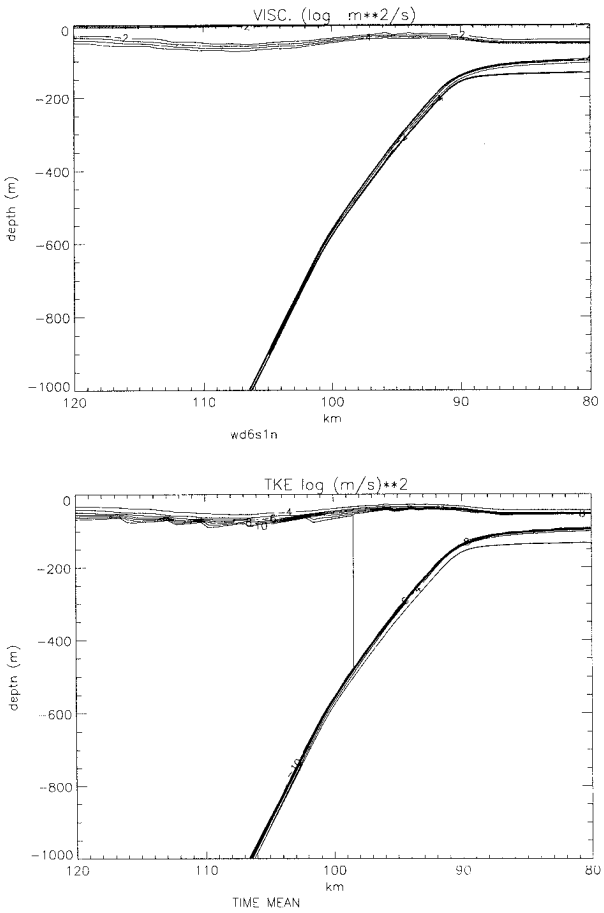

FIG. 7. Contours of (a) $\log_{10}$ of vertical eddy viscosity (m^2 s^{-1}), (b) $\log_{10}$ of turbulence energy (m^2 s^{-2}), produced by an upwelling wind stress condition of 0.2 N m^{-2}.

where ψ_1 and ψ_2 are the Richardson number–dependent stability functions

$$\psi_1 = (1 + 10\text{Ri})^{-1/2} \tag{18}$$

$$\psi_2 = (1 + 3.3\text{Ri})^{-3/2}. \tag{19}$$

In these equations, A_{r1}, B_{r1}, A_{r2}, and B_{r2} are constants; Ri is the Richardson number defined by

$$\text{Ri} = -\frac{\dfrac{gH\partial\rho}{\rho_0\partial\sigma}}{\left(\left(\dfrac{\partial u}{\partial\sigma}\right)^2 + \left(\dfrac{\partial v}{\partial\sigma}\right)^2\right)}. \tag{20}$$

c. Boundary conditions

At the sea surface there is no heat flux, although in the case of wind-driven flow there are wind stresses τ_x, τ_y; thus the boundary condition for temperature and velocity at the sea surface takes the form

$$\frac{\partial T}{\partial\sigma} = 0, \qquad -\rho\frac{K_m}{H}\frac{\partial u}{\partial\sigma} = \tau_x, \qquad -\rho\frac{K_m}{H}\frac{\partial v}{\partial\sigma} = \tau_y. \tag{21}$$

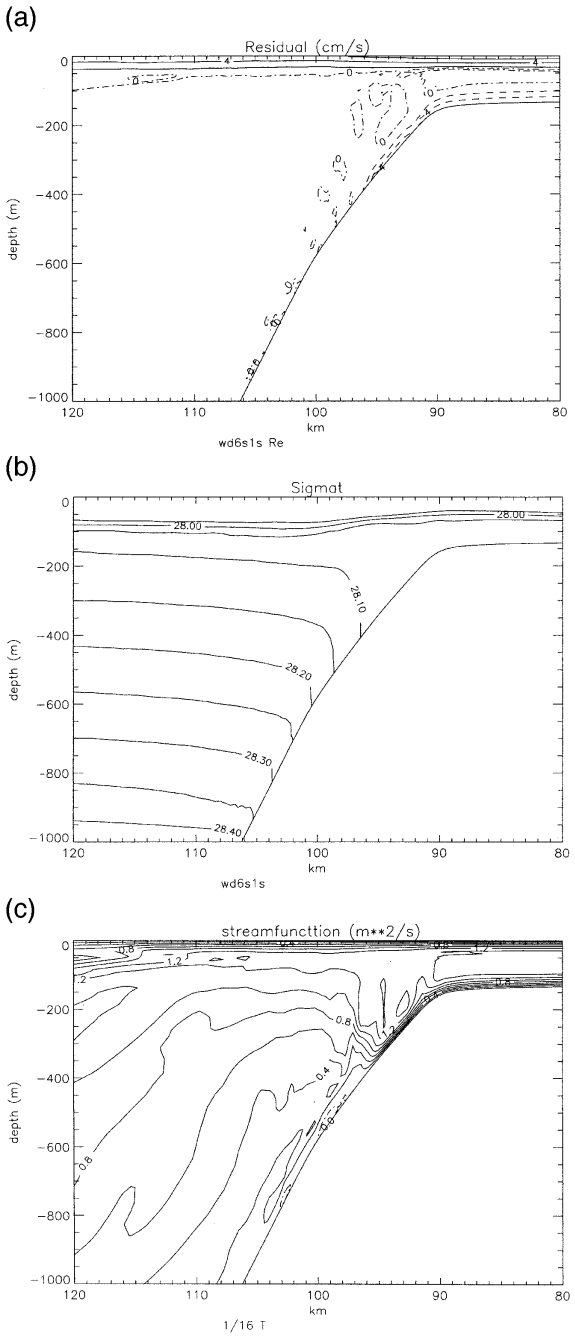

FIG. 8. As in Fig. 6 but for a downwelling wind stress condition of 0.2 N m^{-2}.

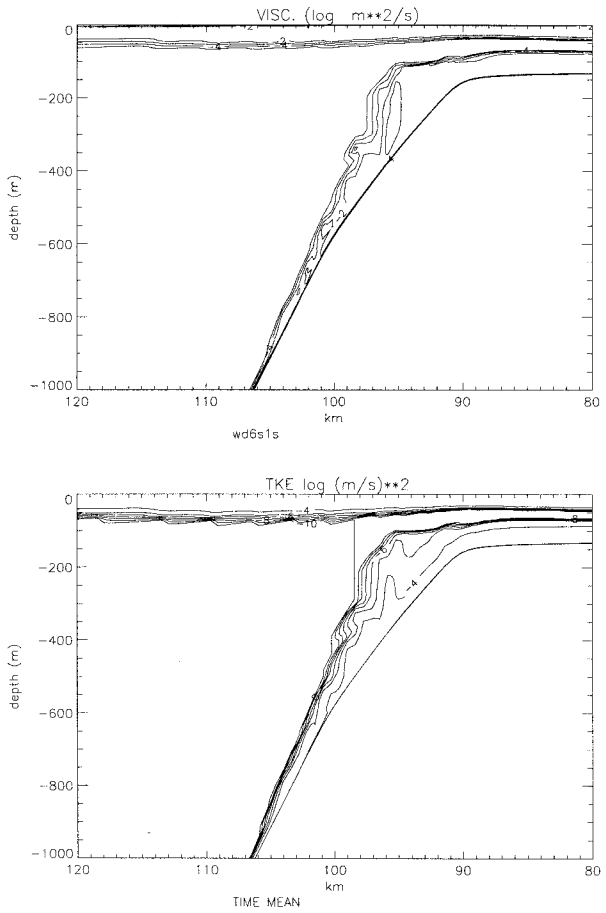

FIG. 9. As in Fig. 7 but for a downwelling wind stress condition of 0.2 N m^{-2}.

At the seabed, a quadratic bottom friction condition is applied of the form

$$K_m\frac{\partial u}{\partial \sigma} = C_d u_h H(u_h^2 + v_h^2)^{1/2},$$

$$K_m\frac{\partial v}{\partial \sigma} = C_d v_h H(u_h^2 + v_h^2)^{1/2}, \qquad (22a)$$

with C_d the coefficient of the bottom friction and u_h, v_h the bottom currents. For the temperature equation there is no flux through the seabed; thus

$$\frac{\partial T}{\partial \sigma} = 0. \qquad (22b)$$

For the q^2–q^2l model, the sea surface boundary condition states that there is no turbulence flux through the sea surface in the absence of wind forcing and takes the form

$$\frac{\partial E}{\partial \sigma} = 0; \qquad (23a)$$

with wind forcing there is a source of surface turbulence given by

$$q^2 = B_1^{2/3}U_{*s}^2, \qquad (23b)$$

where U_{*s} is surface friction velocity and the length scale at the sea surface is given by

$$lq^2 = z_s q^2, \qquad (23c)$$

where z_s is the sea surface roughness length.

At the seabed, we use a boundary condition including

the balance of the turbulence production, dissipation, and diffusion formulated by Xing and Davies (1996b); thus

$$\frac{\partial E}{\partial \sigma} = \frac{C_0 C_1 E^2 H}{\beta_0 K_m^2} + \frac{u_*^4 \delta H}{\beta_0 K_m^2}. \quad (24)$$

Here, δ is the lowest model level height, u_* is the friction velocity with β_0, β_1, and C_0 specified coefficients. A bottom boundary condition for q^2 is formed in a similar way with the length scale specified as the bottom roughness length at the seabed.

In the series of calculations described subsequently the model was applied to a cross shelf x–z transect (Fig. 1), forced at its western open boundary with a barotropic M_2 tide and closed at its eastern boundary corresponding to the coast. A radiation damping type open boundary condition (e.g., Martinsen and Engedahl 1987) was applied at the western boundary to allow waves to be radiated from the region.

d. Parameterization of horizontal diffusion

Calculations were performed using two difference parameterizations of the horizontal diffusion terms, namely the Laplacian form and the biharmonic form, both of which were evaluated on sigma surfaces.

Considering the term F_u for illustrative purposes (with F_v and F_T formulated in a similar way), then the Laplacian form is given by

$$F_u = A_M \nabla^2 u = A_M \left(\frac{\partial^2 u}{\partial x^2} + \frac{\partial^2 u}{\partial y^2} \right) \quad (25)$$

with the biharmonic form given by

$$F_u = -B_M \nabla^4 u = -B_M \left(\frac{\partial^4 u}{\partial x^4} + 2\frac{\partial^4 u}{\partial x^2 \partial y^2} + \frac{\partial^4 u}{\partial y^4} \right) \quad (26)$$

with A_M and B_M, coefficients for horizontal momentum diffusion, taken as constant. Identical values were used for the heat and turbulent energy diffusion coefficients (A_H and B_H).

e. Numerical solution

Since extensive details of the numerical solution have been presented previously in the context of three-dimensional shallow sea models with density either uniform or specified diagnostically (i.e., excluding internal tides) (Davies and Xing 1995; Xing and Davies 1996a,b,c), only a very brief indication will be given here. A finite-difference grid of the order of 50 sigma levels was used in the vertical, with enhanced resolution in the near surface and bed layers, in order to resolve the higher vertical shear that occurs in these regions. A staggered Arakawa C-grid was applied in the horizontal. From a series of calculations using idealized topography, in which numerical solutions are compared with the analytical solutions of Craig (1987), Xing and Davies (1996d) found that an across-shelf grid resolution of the order of 0.625 km was necessary in order to accurately resolve the internal tide. Although no wind effects were included in these calculations, which were primarily concerned with numerical accuracy, and the idealized topography used by Craig (1987) was employed, the conclusions of the paper concerning the need to use a fine grid of the order of 0.625 km appear valid here, and a grid of this resolution was employed in all calculations. At the seabed a quadratic slip condition was applied with a drag coefficient corresponding to a bed roughness length $z_0 = 0.005$ m. The use of a slip condition enables the hydrodynamic equations to be integrated using a time split approach (Xing and Davies 1996a), with the external mode being integrated using a time step of 2.79 sec, and the internal modes with a time step of 111.785 sec. (A 40 to 1 time split of the internal to surface time step.) An implicit method was used to discretize the vertical diffusion terms, with the horizontal diffusion terms being computed explicitly.

A central differencing method was used for momentum advection, although a total variation-diminishing (TVD) (James 1996) scheme was found in a detailed series of numerical calculations concerned with the advection of density over steep topography (Xing and Davies 1996d) to be essential for the advection of temperature and density.

3. Internal tide and wind calculations

In this series of calculations we examine the influence of upwelling- and downwelling-favorable winds of magnitude 0.2 N m^{-2} upon the amplitude of internal tidal currents and displacements in the shelf slope region off the west coast of Scotland at 57°N. This region is chosen because it is the area of a planned oceanographic field experiment and previous numerical calculations have been performed to examine the internal tide in this region, using an extensive range of parameterizations of subgrid-scale mixing (Xing and Davies 1996e), although without the influence of wind events. To the authors' knowledge this is the first time the influence of wind-driven flows upon the internal tide has been examined. An idealized cross-section model is considered, consisting of a shelf of 90-km width, connected to a physically realistic shelf slope, with a constant depth ocean to the west (Fig. 1). The model is forced with an M_2 barotropic tide at its western open boundary, which is typical of the region (Xing and Davies 1996a), giving a peak tidal current of 25 cm s^{-1} at the shelf break decreasing to a coastal value of zero (Fig. 1). The model was integrated forward in time from an initial state in which an observed (Ellett et al. 1986) typical winter temperature profile (Fig. 2) was specified. This profile is identical to that used by Davies and Xing (1996e).

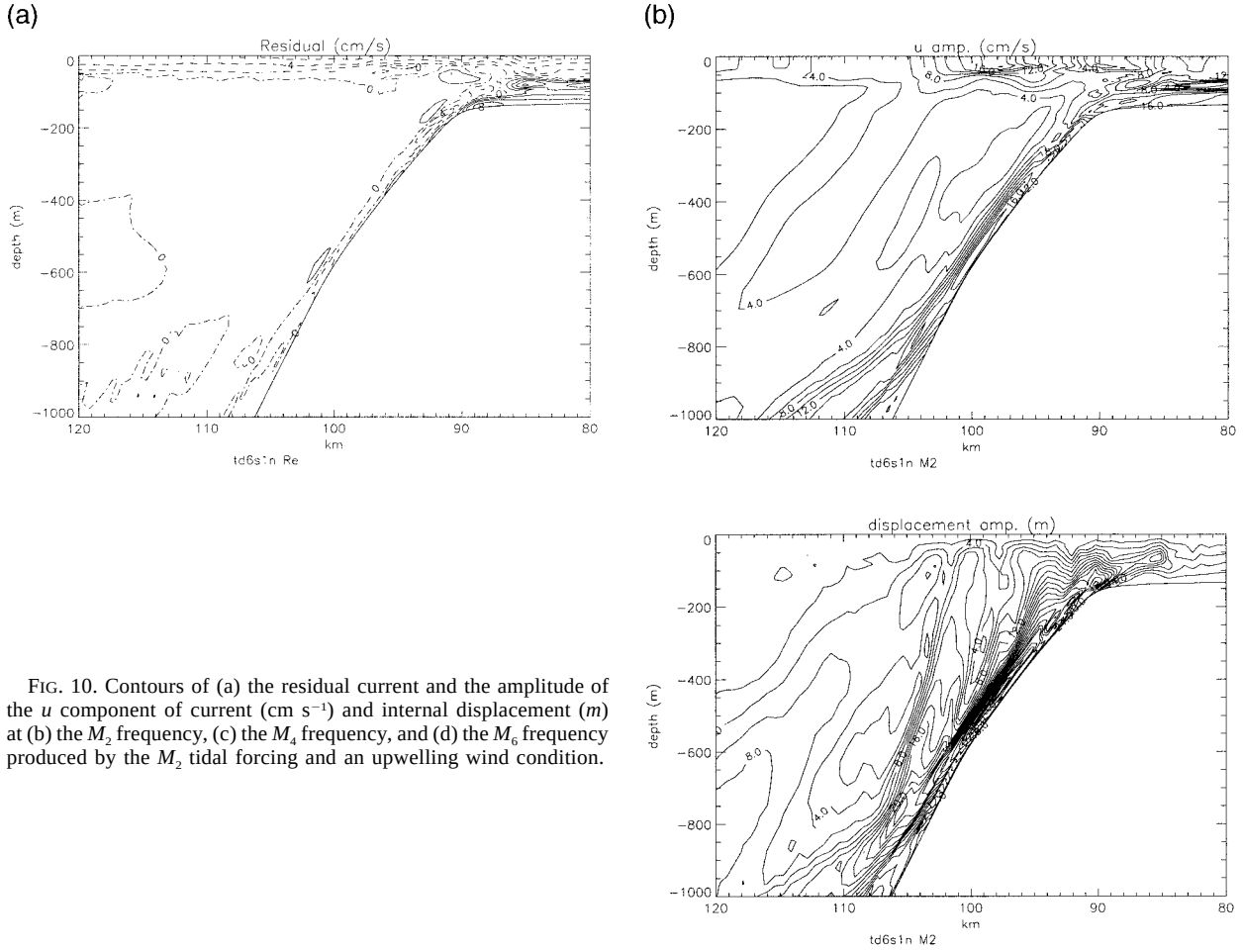

FIG. 10. Contours of (a) the residual current and the amplitude of the u component of current (cm s^{-1}) and internal displacement (m) at (b) the M_2 frequency, (c) the M_4 frequency, and (d) the M_6 frequency produced by the M_2 tidal forcing and an upwelling wind condition.

a. Calculations using the q^2–q^2l turbulence model

1) TIDAL CALCULATIONS

In an initial calculation (calculation 1, Table 1) the model was integrated through time for 30 tidal cycles with only the M_2 barotropic tidal forcing in order to remove the effects of the initial elevation and current conditions, and results were saved over an M_2 tidal period for harmonic analysis. In this calculation the two-equation q^2–q^2l model was used to determine the vertical mixing of momentum and density. Calculations were performed using both the Laplacian and biharmonic form of horizontal diffusion with $A_M = 5$ m^2 s^{-1} and $B_M = 5 \times 10^5$ m^4 s^{-1}, a comparable biharmonic value (Heathershaw et al. 1994). With these values, the horizontal diffusion term was small and there was no noticable difference in the computed results. For reasons of computational economy and to be consistent with earlier calculations the Laplacian form was used in all subsequent calculations.

Since a detailed study of the internal tide, using a range of subgrid-scale mixing formulations but without wind effects, has been given in Xing and Davies (1996e), we will only present the aspects of the calculation relevant to an understanding of how the tide is modified by wind forcing.

Contours of the amplitude of the u component of the internal tidal residual current and the current and internal displacement at the M_2 frequency and its higher harmonics, namely, M_4 and M_6, are given in Figs. 3a–d. The residual and the various tidal harmonics were obtained by a harmonic analysis of the last of the 30 tidal cycles over which the model was integrated. The tidal residual and higher harmonics are generated by the nonlinear terms in the model, which move energy from the forcing frequency into the other frequencies. (It is important to note that the currents shown here are due to the internal tide only, with the total tidal current being the sum of the depth-mean tidal current induced by the barotropic tide and those shown here.)

The vertical variation of the tidal current shown here is therefore due to both the internal baroclinic pressure gradients, which act throughout the water column, and internal viscous effects, in particular the bottom stress, which is responsible for reducing the current in the near-

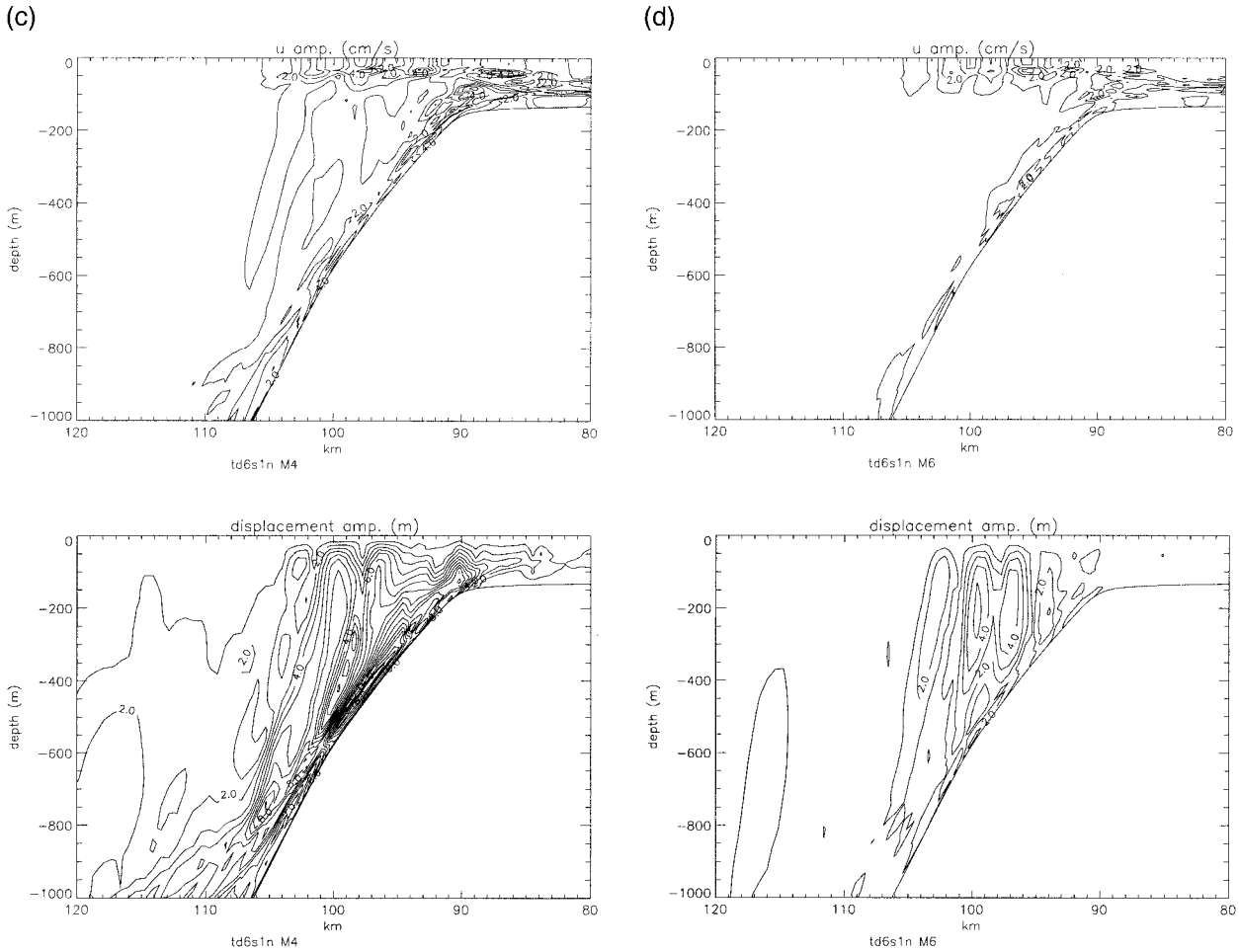

FIG. 10. (*Continued*)

bed region. A detailed discussion of this effect is given in Xing and Davies (1996d) and is not repeated here.

Although we will mainly be concerned with examining the coupling between the wind and the internal tide in terms of the modification of the fundamental and higher harmonics of the internal tide, in an analogous manner to the shallow sea study of Davies and Lawrence (1994) in connection with the barotropic tide, there are other approaches (New and Pingree 1990; Lamb 1994) available for examining tidal calculations. These other methods, which have been used in tide only calculations, involved a decomposition using eigenfunctions of the buoyancy frequency in the vertical. Such an approach is valid for the internal tide alone, where the buoyancy frequency averaged over the tidal cycle remains unchanged. However, as we will show later with upwelling and downwelling wind conditions, the density profile in some regions can change significantly making such a comparison of solutions with and without wind forcing very difficult.

Contours of the residual tidal current (Fig. 3a) show a region of near-surface positive tidal residual having an amplitude of the order of 2 cm s^{-1} above the shelf break, with stronger near-surface residual currents in the opposite direction on the shelf. At the top of the shelf slope is a region of strong near-bed tidal residuals with a magnitude of about 6 cm s^{-1}. Comparing Figs. 3a with 3b, it is evident that the region of strong near-bed tidal residuals coincides with the region where the near-bed M_2 tidal currents reach a maximum with similar correlations at other locations.

Regions of intensified M_2 tidal current amplitude and displacement (Fig. 3b) at the seabed along the slope and sea surface, associated with positions where the internal tide is generated in the near-bed region, and its subsequent propagation along internal ray paths (New 1988; New and Pingree 1990; Sherwin 1988, 1991; Sherwin and Taylor 1989, 1990) are clearly evident in both the contours of current magnitude and internal displacement (Fig. 3b). It is evident from these figures that the region of maximum internal tide generation is located on the shelf slope between 105 and 95 km offshore with the internal tide propagating downslope and off the shelf from this position, although some does propagate onto

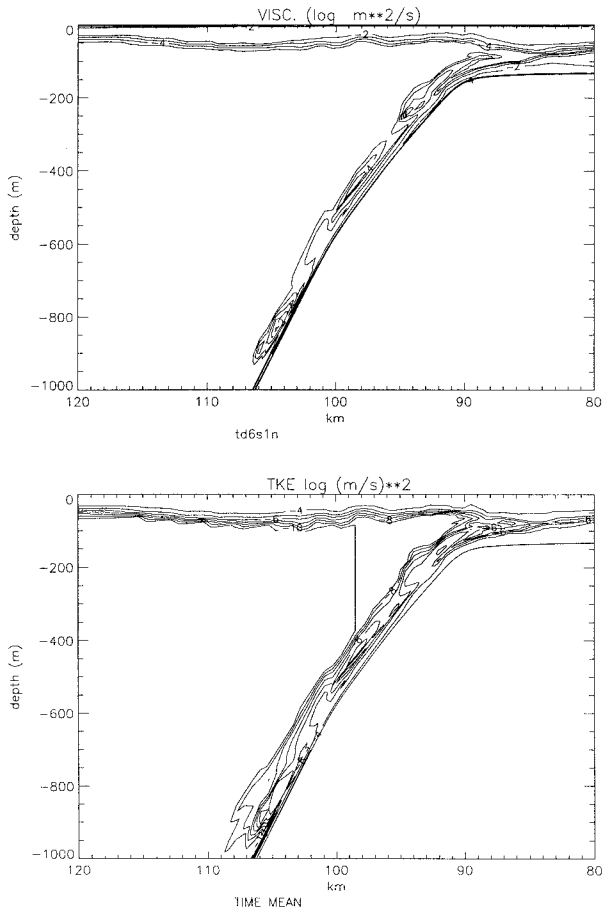

FIG. 11. Contours of the time average over an M_2 period of (a) $\log_{10}$ of vertical eddy viscosity ($m^2\ s^{-1}$), (b) $\log_{10}$ of turbulence energy ($m^2\ s^{-2}$) produced by the M_2 tidal forcing, and an upwelling-wind condition.

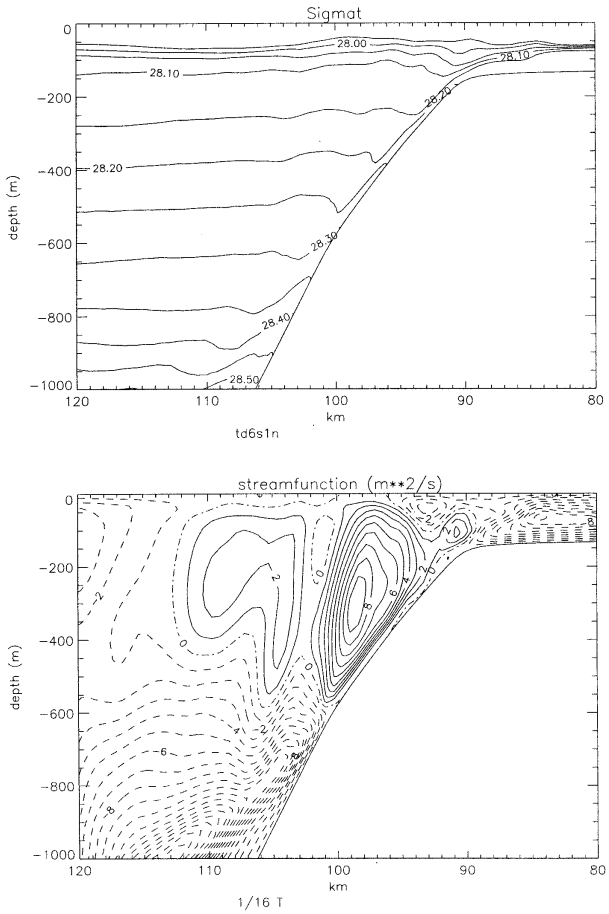

FIG. 12. Contours over an M_2 tidal cycle T of sigma-t (σ_t) and the streamfunction at the top of the shelf slope induced by the M_2 tide and an upwelling-favorable wind.

the shelf. (A detailed discussion of the mechanisms generating the internal tide is given in Xing and Davies (1996d) and is not repeated here). Contours of the amplitude of the u component of the M_4 tide, and its internal displacement are given in Fig. 3c. Comparing Figs. 3c with 3b it is apparent that the location of the regions of strongest M_4 signal occur at the same positions as those of the M_2 tide. This is to be expected since in these regions the change in the tidal currents, and also the internal displacement, is a maximum and hence the nonlinear term responsible for producing the M_4 tide is a maximum. Since a significant contribution to the M_6 tidal current is through bottom frictional effects, this component shows a maximum near-bed current (Fig. 3d) at the top of the shelf slope where the M_2 bed currents are large, with an associated area of maximum internal displacement (Fig. 3d). Changes in the location and magnitude of these features due to wind effects will be considered in subsequent calculations.

Besides considering the spatial distribution of the internal tidal currents and displacements, it is valuable to examine the distribution of vertical viscosity and turbulence energy at the top of the shelf to determine how they change when wind effects are included. Contours of the time mean (over an M_2 tidal cycle) of these quantities derived from the tide-only calculation are given in Fig. 4. The turbulent kinetic energy at the top of the shelf break shows significant spatial variability in the near-bed region corresponding to the locations of maximum amplitude in the near-bed tidal currents. Also evident are regions of intensified surface turbulence energy corresponding to the areas of increased surface current. Areas of increased eddy viscosity and diffusivity are associated with these regions of intensified turbulence energy.

To understand the spatial variability of the internal tidal currents and displacements at the various frequencies—namely, M_2, M_4, and M_6—the associated turbulence energy, and changes produced by adding wind forcing, it is useful to examine variations in the density field (here given by σ_t contours where $\sigma_t = \rho\ (\text{kg m}^{-3}) - 1000$ and the associated streamfunction over a tidal cycle (Fig. 5). (The conventional notation of the streamfunction used here is such that a continuous line is a

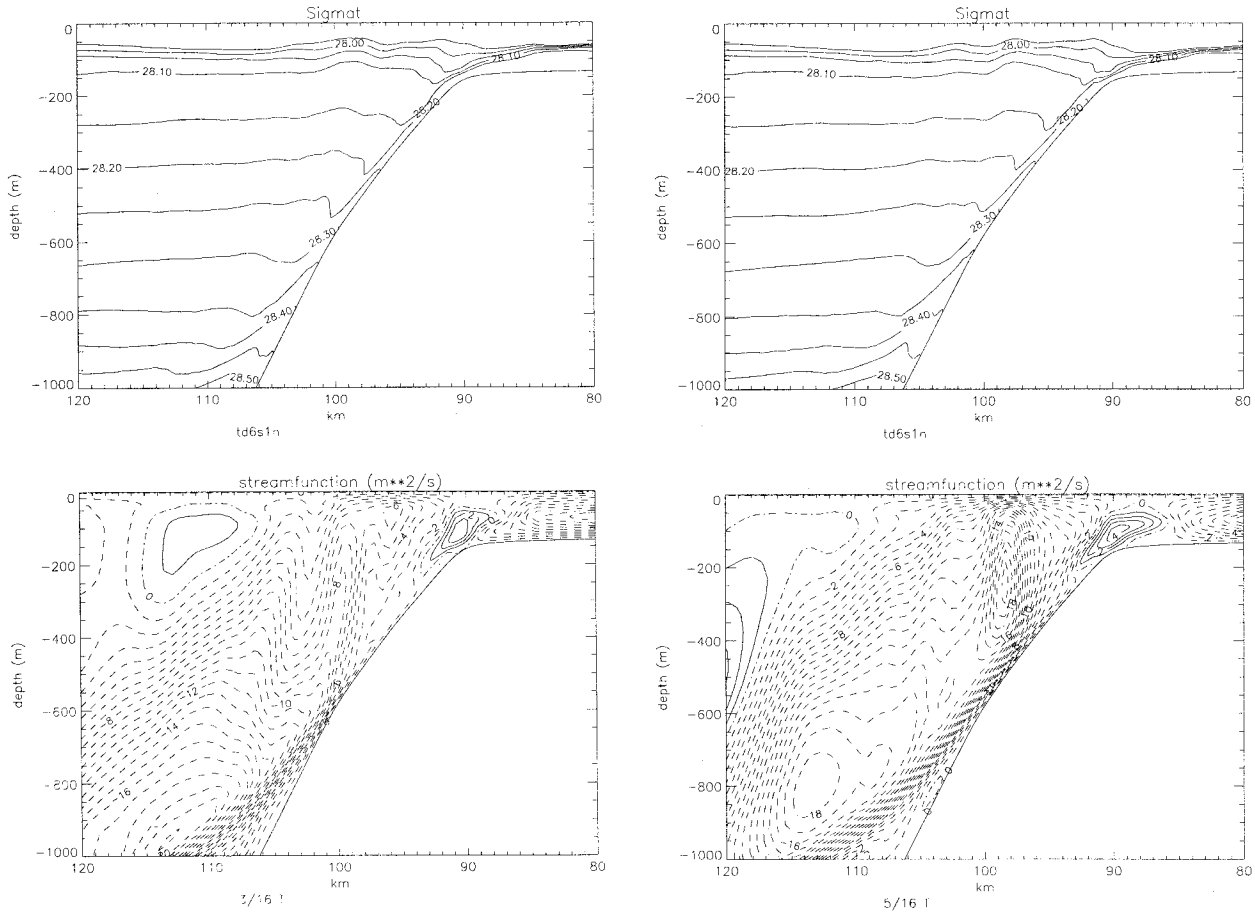

FIG. 12. (*Continued*)

positive value, a dashed line negative, and a dashed and dotted line is zero. A region of clockwise circulation occurs along contours enclosing a maximum, with anticlockwise along contours enclosing a minimum). It is not the intention here to give a detailed account of the processes influencing the spatial and temperal changes in the density field, as this is considered in detail in Davies and Xing (1996d–f), but rather to present the main features so that changes produced by adding wind forcing to that of tidal origin can be separated from those due to the tide alone.

Considering initially the distribution of density surfaces at $t = (1/16)T$ (where T is the M_2 tidal period), after the model has been integrated for 30 tidal cycles, there are some significant displacements of the density surfaces associated with large amplitude internal waves along the shelf slope region between 400 and 900 m. These large displacements are mainly confined to the shelf break region, with only small variations appearing 120 km from the coast (Fig. 5). At the top of the shelf break where bottom turbulence is large, enhanced mixing occurs and downwelling of the $\sigma_t = 28.10$ surface is evident and can be seen in the streamfunction contours. Above this surface in the near-surface layer (upper 100 m) where vertical stratification is strong, short wavelength internal waves are generated by the nonlinear processes in the model. [A detailed discussion of this phenomenon is given in Xing and Davies (1996e, f) and is not repeated here.]

Contours of the density surfaces and the associated streamfunction at $t = (3/16)$T, $t = (5/16)T$, and $t = (6/16)T$ show an upwelling along the upper part of the shelf slope, and associated with this the internal waves in the surface layer above the shelf break show increased steepening. A recent numerical modeling study (Lamb 1994) also found short waves of the form shown here above the shelf break, and observational evidence (Holloway 1984, 1996; Heathershaw et al. 1987) exists to support their occurrence. A detailed discussion of the nonlinear mechanisms responsible for the generation of these short period waves is given in Xing and Davies (1996d) and is not discussed here. These nonlinear terms are responsible for generating the higher tidal harmonics in the shelfbreak region.

The downwelling region at depth, evident (Fig. 5) at $t = (6/16)T$ (namely the distribution of the streamfunction below 800 m), progresses farther up the shelf slope as the internal tide reverses and by $t = (8/16)T$, downwelling

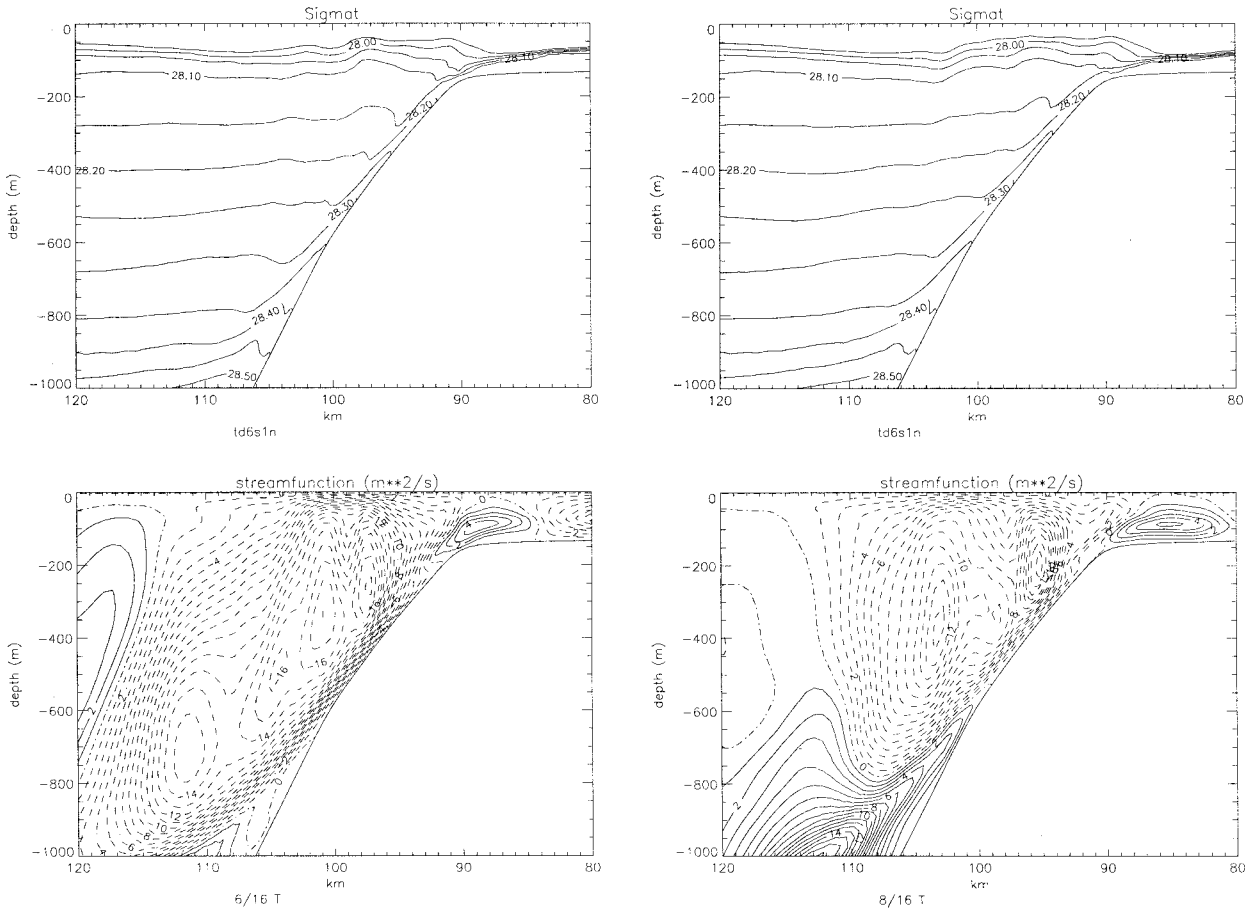

FIG. 12. (*Continued*)

occurs along the shelf slope below 500 m, producing a downward movement of the $\sigma_t = 28.25$ contour in the layer just above the seabed, although the $\sigma_t = 28.20$ surface continues to upwell.

The influence of wind-induced upwelling and downwelling upon these distributions will be considered in the following sections. However, before examining this it is necessary to consider the effects of downwelling and upwelling wind conditions upon the currents and density fields at the shelf break.

In these calculations we have chosen typical winter stratification and mean wind stresses. However, the results are generally applicable and are relevant for summer stratification (which is stronger in the seasonal thermocline), although winds are weaker. However, in the case of strong stratification and strong winds—a summer wind event, the resulting coupling might be larger than shown here. Also, in the calculations presented here we assume a steady time-independent wind stress, which would not occur in reality. However, as we are primarily concerned with a process study rather than a comparison with detailed measurements, the assumption of a steady wind stress is valid and enables the results to be more readily interpreted.

2) UPWELLING FAVORABLE WIND

In order to understand the interaction of the internal tide and the oceanic response to wind, it is necessary initially to examine the effect of the wind only. To do this the previous calculation was repeated (calculation 2, Table 1) using an identical initial density field and integration period but with forcing produced by a constant upwelling-favorable wind stress of -0.2 N m^{-2}, a typical mean wind stress over the winter.

This wind stress causes an off-shelf flow in the surface layer (Fig. 6) with a compensating upwelling in the upper part of the shelf slope giving rise to the upward sloping sigma-t surfaces in Fig. 6. The upwelling currents at the seabed along the shelf slope, running over a rough bed, give rise to increased turbulence intensity (Fig. 7), producing a region of enhanced vertical eddy viscosity and diffusivity. The increased mixing in the seabed region, particularly near the top of the shelf slope, leads to the generation of a thin well-mixed bed layer (Fig. 6) and is responsible for the very rapid change in the density field near the top of the shelf break.

Obviously the upwelling of the density fields will continue until the internal pressure gradients oppose it.

A detailed descussion of this balance is beyond the scope of the present paper but is considered using an idealized analytical model in MacCready et al. (1993), who also give a timescale to reach a steady state. The upwelling found here is similar to that shown by MacCready et al. (1993) except that, since the present model contains vertical diffusion terms which are large in the near-bed region, it produces the sharp near-bed density gradients associated with enhanced bottom mixing. Also, since the present model allows for vertical mixing, it may not reach a steady state (other than that occurring when the water column is completely mixed).

Besides increased bed mixing associated with the upwelling currents flowing over a rough bottom, there is increased turbulence energy and mixing in the surface layer (Fig. 7) produced by wind-induced turbulence and shear in the water column, which has an influence upon the near-surface density field. That both the surface density field and, in particular, the gradient of the near-bed density field have been significantly changed by the wind forcing suggests that the internal tide will be significantly influenced by wind events. A detailed examination of this will be given after we have examined the effect of a downwelling wind condition.

3) DOWNWELLING-FAVORABLE WIND

The influence of a downwelling-favorable wind was examined by repeating the previous calculation but with a constant downwelling-favorable wind stress of $+0.2$ N m^{-2}. This gives rise to an onshelf flow in the surface layer with currents of the order of 4 cm s^{-1} (Fig. 8), and a return flow in the near-bed layer on the shelf and at the top of the shelf slope having a similar magnitude. Associated with this flow the streamfunction (Fig. 8) shows a significant downwelling at the top of the shelf slope. The effect of the strong downwelling in this region is to move lighter water down the slope, giving rise to intense vertical mixing (Fig. 9) at the top of the shelf slope. This increased mixing at the top of the shelf slope produces the significant downward displacement evident for the $\sigma_t = 28.10$ surface (Fig. 8). At greater depths, for example 600 m below the surface, streamfunction contours show that the downward velocity is quite small, and the displacement of the density surface is reduced although bottom mixing changes the density profile in the near-bed region. However, if the model is integrated for a longer period of time, the intense mixing at the top of the shelf slope penetrates farther down the slope and a shelf edge front forms between a mixed region along the slope and a stratified oceanic area. A detailed discussion of this phenomenon is beyond the scope of the present paper, although the behavior of the model is very similar to the anlytical solutions derived by MacCready et al. (1993).

Comparing contours of turbulence energy and eddy viscosity (Fig. 9) computed for a downwelling-favorable wind with those for an upwelling-favorable wind (Fig. 7), there is no significant difference in the near-surface layer where wind-induced turbulence dominates. With the downwelling wind condition however, the turbulence energy intensity and mixing coefficients are significantly larger and the region of increased bed turbulence extends much farther into the water column. The reason for the increased thickness of the bottom turbulent layer in this case is that the strong vertical density gradients, which exist in the upwelling case and suppress the turbulence, are not present in the downwelling situation. As in the previous calculation the wind has made a significant difference to the near-bed density gradients, and hence changes in the internal tide can be anticipated and will be discussed subsequently.

4) UPWELLING-FAVORABLE WIND AND TIDAL FORCING

In this calculation (calculation 4, Table 1) the model was integrated through time for 30 tidal cycles with both M_2 tidal forcing and an upwelling wind stress of -0.2 N m^{-2}, and results were saved over an M_2 tidal cycle and subsequently analyzed.

Contours of the u component of the residual current (due to both wind and internal tide) and the current amplitude and internal displacement at the M_2 frequency and its higher harmonics namely M_4 and M_6 (Figs. 10a–d). The residual current (Fig. 10a) at the sea surface away from the shelf break is not significantly different from that induced by the wind alone (Fig. 6); this result is to be expected since in this area the tidal residual (Fig. 3a) and the nonlinear terms are small. However, at the top of the shelf slope and on the shelf, the residual flow is significantly different to that produced by the wind only, reflecting the effect of the tidal residual and the importance of the nonlinear terms there.

Comparing contours of the amplitude and displacement of the M_2 tide computed with wind forcing (Fig. 10b) and without (Fig. 3b), it is evident that although the spatial distribution of the current amplitude is similar, in that a region of enhanced M_2 tidal current at the sea surface occurs in both cases at approximately 100 km off shore, the area of increased bed currents has moved farther down the slope from a water depth of the order of 425 m, to a depth of nearly 600 m, indicating that the position on the slope where the internal tide is generated has changed. This result is to be expected since the location of the point at which the internal tide is generated depends critically upon the shelf slope and local density gradient, which has changed significantly due to the upwelling produced by the wind. This phenomenon will be considered in more detail later in this paper.

From a comparison of the contours of the internal displacement of the M_2 tide (cf. Fig. 3b with Fig. 10b) it is evident that the internal displacement at the top of the shelf break in the near-bed region has been significantly influenced by the change in density field pro-

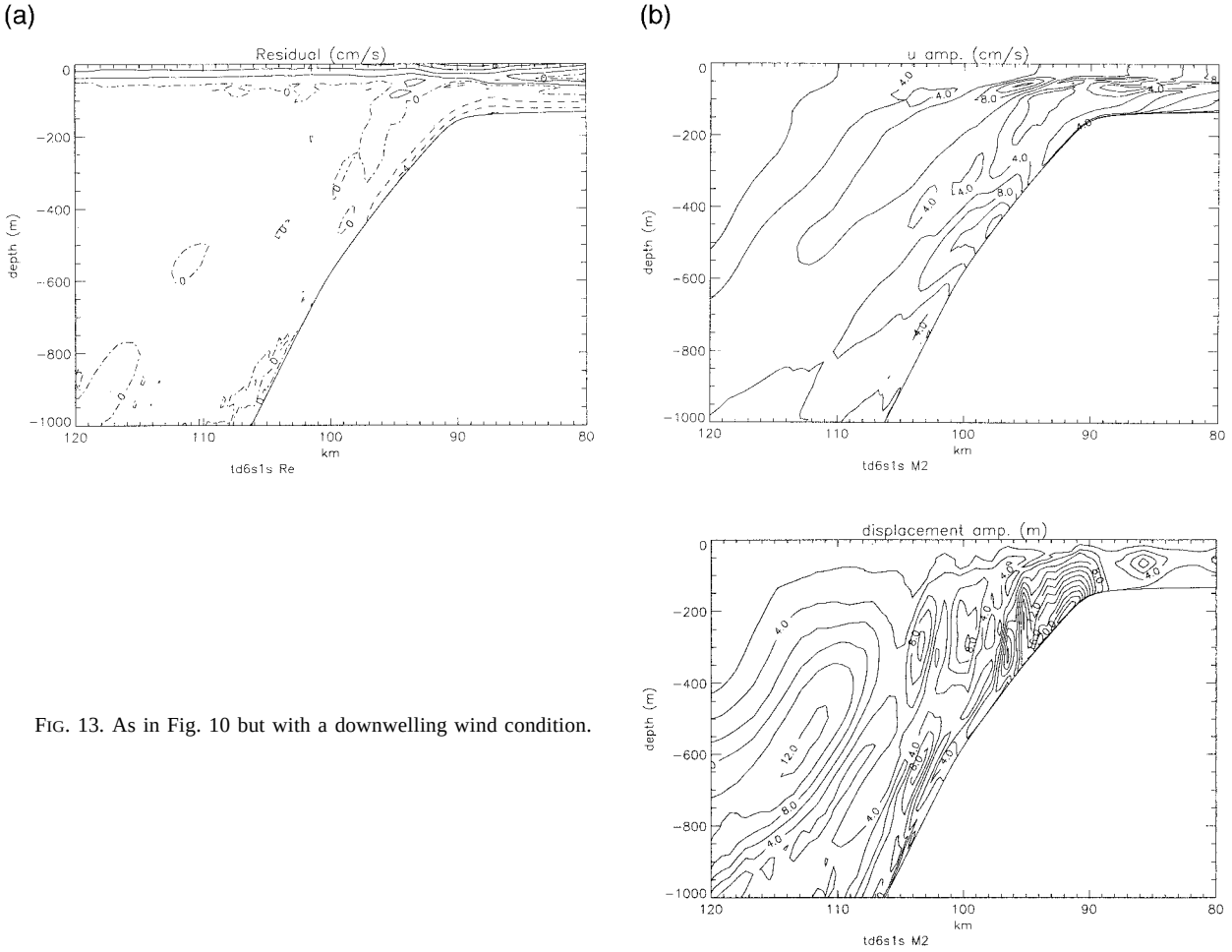

FIG. 13. As in Fig. 10 but with a downwelling wind condition.

duced by the wind. Changes are also evident on the shelf, with some slight differences in the open ocean.

Considering the M_4 component of the tide (Fig. 10c), a comparison of the current amplitudes with and without the wind (cf. Figs. 3c with 10c) shows that the wind has affected the spatial distribution of the current amplitude of the second harmonic of the internal tide. Also there are significant changes in the magnitude and spatial distribution of the internal displacement, the reasons for which will be considered later. Significant changes are also evident in the M_6 component of the internal tide, with an increase in current amplitude (compare Fig. 3 with Fig. 10) and also significantly larger spatial variability in the surface and bed layers. A similar increase in magnitude of the internal displacement at the M_6 frequency when the wind is included compared with the tide only solution is also evident from a comparison of the internal displacements.

Comparing contours of turbulent kinetic energy and viscosity averaged over an M_2 tidal period, as shown in Fig 11, with those determined with a northerly wind only (Fig. 7) and tide only (Fig. 4) it is evident that in the surface layer at distances over 110 km from the coast, the contours are not significantly different from those due to the wind only. Above the shelf break and on the shelf there are some differences from the wind only solution due to enhanced mixing produced by the internal tide (Fig. 4). On the shelf for the tide and wind solution (Fig. 11), surface and bed boundary layers overlap due to increased turbulence produced by the wind and the tide, with the bed boundary layer at the top of the shelf break being significantly thicker than in the wind-driven flow case due to the enhanced turbulence produced by the tide.

To understand these differences in turbulent mixing and the changes produced by the wind in the internal tidal displacement, particularly for the higher harmonics, it is instructive to examine contours of σ_t and the streamfunction (Fig. 12) for an identical tidal period to that considered previously (Fig. 5). Considering initially contours of σ_t at $t = (1/16)T$, where T is the M_2 tidal period after the model has been integrated forward in time for 30 tidal cycles, it is evident from Figs. 12 and 5 that the most significant difference is the strong upwelling of the density contours along the shelf slope due to the wind (Fig. 6). Away from this bottom bound-

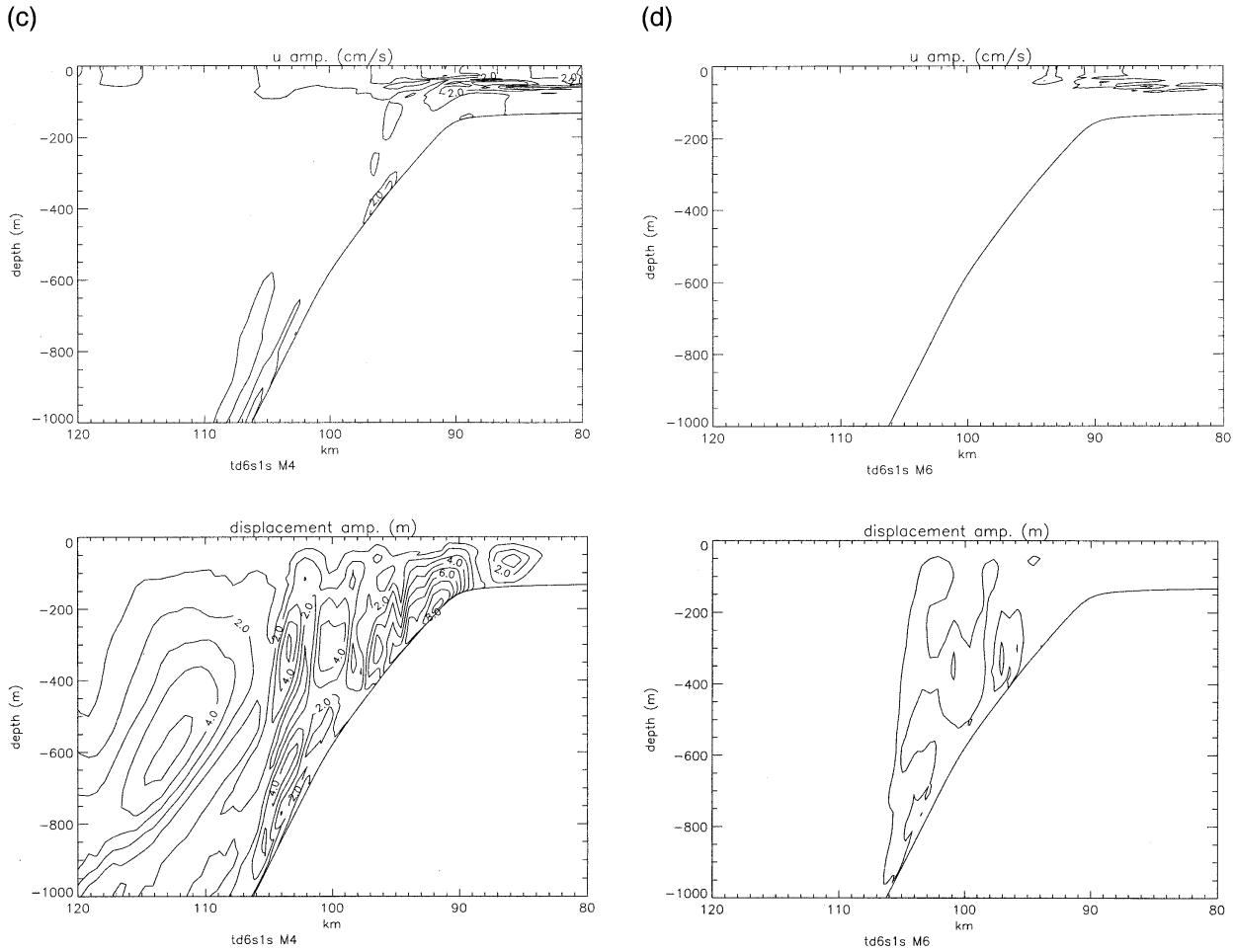

FIG. 13. (*Continued*)

ary layer and in the surface layer, oscillations in the density surfaces are clearly evident due to the internal tide, showing similar spatial variability to that found in the tide only solution (compare Fig. 12 and Fig. 5).

Contours of the streamfunction (Fig. 12) show a region of strong upwelling along the shelf slope at a depth of 400 m associated with the wind-driven upwelling, which is not present in the tide-only solution (Fig. 5). At a later time, namely, $t = (\frac{3}{16})T$, streamfunction contours show that the upwelling area at a depth of 400 m has been replaced by a weak downwelling flow (Fig. 12). The reason for this reversal is that at this time downwelling is associated with the internal tide (Fig. 5) and the tidal currents are opposing the upwelling currents associated with the wind forcing.

The upwelling at depths of 400 m produced by the wind is evident at $t = (\frac{6}{16})T$ with a region of downwelling due to the internal tide at this time at the top of the shelf break. This region of rapidly changing upwelling and downwelling at the top of the shelf slope gives rise to significant spatial variations in the density field, which appear as the short internal waves evident in Fig 12 [$t = (\frac{6}{16})T$] at this time. Similar although spatially more uniform short period waves are present at this time at the top of the shelf slope in the tide only solution (Fig. 5, $t = (\frac{6}{16})T$] due to the nonlinearity in the solution. The differences between the two solutions, and the significantly larger variability in both the instantaneous density field and the M_4 and M_6 analysis of the internal displacements in the tide plus wind solution, are due to the increased density gradient at the top of the shelf slope and hence the increased importance of the nonlinear terms, which produce these small-scale features on the density field.

At a subsequent time, namely, $t = (\frac{8}{16})T$, downwelling occurs along the shelf slope at depths below 600 m due to the currents associated with the internal tide in this region (Fig. 5). However, the tidally induced downwelling that occurs in the tide-only solution at 400 m (Fig. 5) is suppressed by the wind-induced upwelling at this location (Fig. 6) and the density surfaces continue to upwell at this depth, producing significantly larger displacement and, hence, internal waves along the $\sigma_t =$

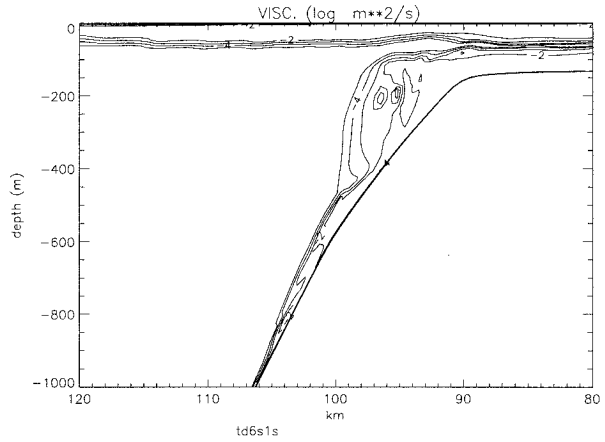

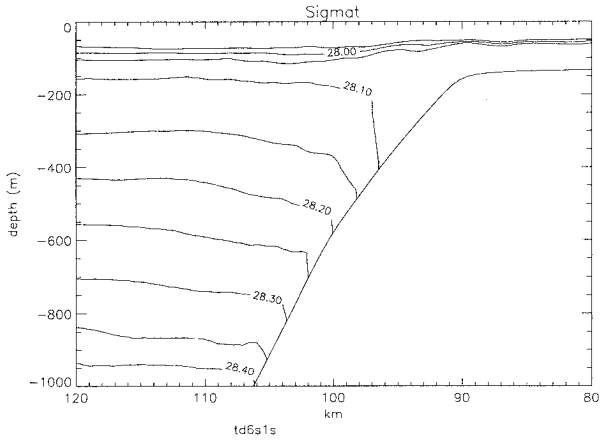

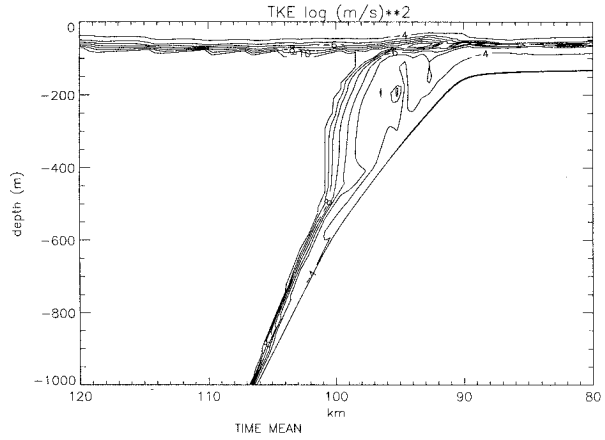

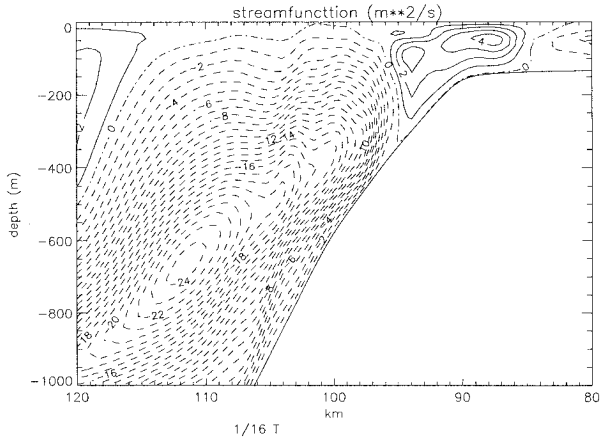

FIG. 14. As in Fig. 11 but with a downwelling wind condition.

FIG. 15. As in Fig. 12 but with a downwelling-wind condition.

28.15 surface (Fig. 12) than those found in the tide-only solution (Fig. 5).

This detailed examination of the time variability of the internal density surfaces and the associated streamfunction gives some indication of the reasons for the differences in amplitude of the internal tidal currents and displacements produced by wind-induced upwelling.

Besides changes in the density field produced by its advection by the internal tide and the wind, the present model also contains the density diffusion terms, which on the longer timescale will also modify the density field. Obviously all modifications of the density field, but particularly those in regions of critical slope, will influence the propagation of the internal tide and, hence, both its distribution along the slope, together with off-shelf and on-shelf regions, as shown here from a comparison of Fig. 5 and Fig. 12, although the effect upon the distribution of σ_t surfaces in the open ocean (of order 120 km from shore) is significantly less than at the shelf slope.

5) DOWNWELLING-FAVORABLE WIND AND TIDAL FORCING

In this section we consider the coupling of a downwelling wind condition and tidal forcing (calculation 5, Table 1). As in the previous calculation, the model was integrated through time for 30 tidal cycles with both M_2 tidal forcing and in this case a downwelling wind stress of $+0.2$ N m^{-2}; results saved over a tidal cycle for harmonic analysis.

Contours of the u component of the residual current (Fig. 13a) at the sea surface and the seabed to the west of the shelf break are not significantly different from those found with wind forcing alone (Fig. 8), although there are some slight differences in the surface currents above the shelf break and on the shelf (cf. Figs. 13 and 8), where the tidal residual is significant (Fig. 3). Comparing contours of the M_2 tidal current amplitude and displacement computed with and without the wind forcing (Figs. 13 and 3), it is evident that the internal tidal current magnitude at the sea surface and seabed and the internal tide displacement have been significantly reduced by the downwelling wind (cf. Fig. 3 with Fig. 13). Such significant changes with the downwelling wind are to be expected since this wind produces significant mixing along the upper part of the shelf slope (Fig. 8) as described. previously, which produces a change in the local density field such that density gra-

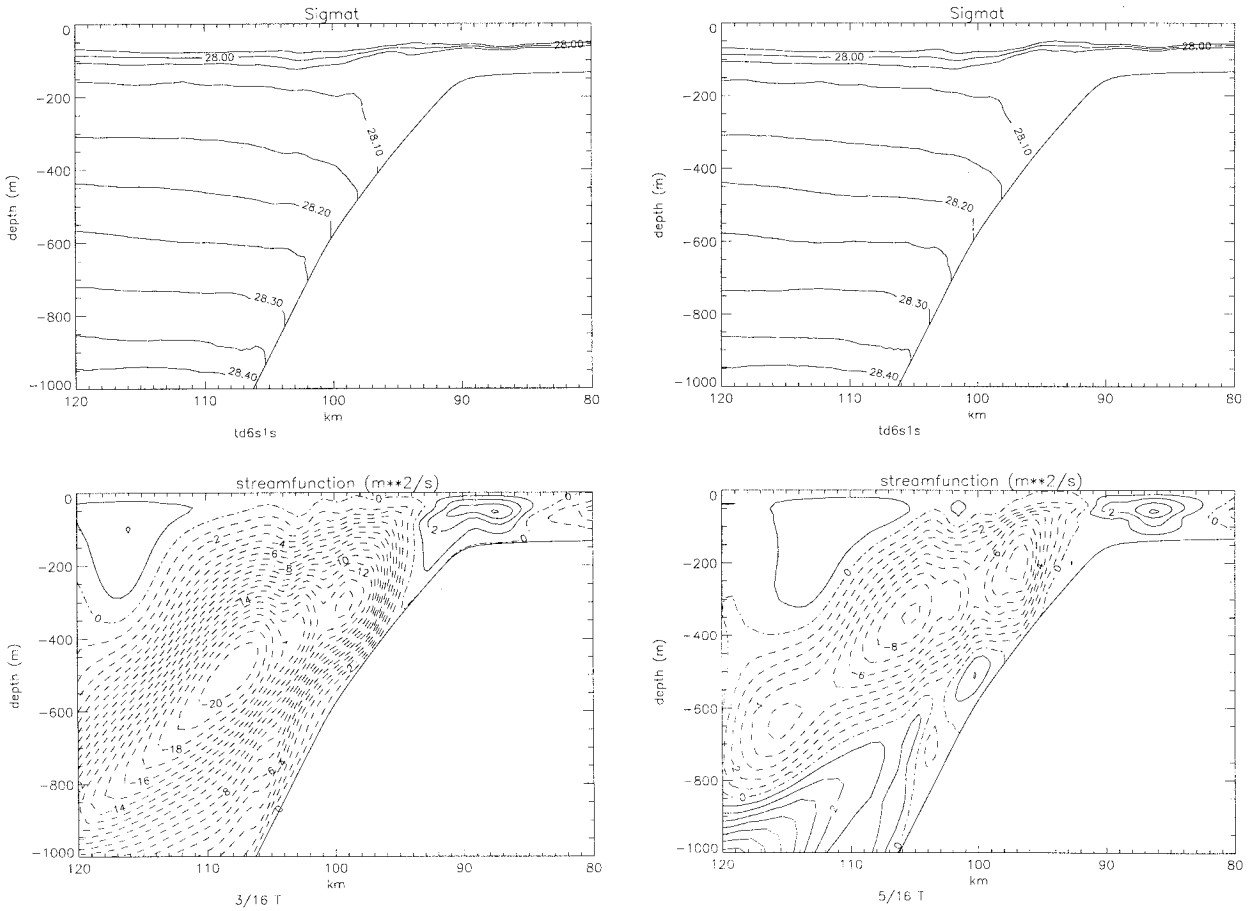

FIG. 15. (*Continued*)

dients are reduced, leading to a decrease in the internal tide amplitude.

From a comparison of currents and displacements of the M_4 component of the tide with and without wind forcing (Figs. 13c and 3c) it is evident that the magnitude of M_4 currents and displacements along the shelf slope and in the upper part of the water column have been reduced by including wind effects. A similar examination shows that with a downwelling wind condition, little or no internal tide at the M_6 frequency was generated. These changes can, in part, be understood from an examination of the changes in the density field produced by a downwelling-favorable wind (Fig. 8). As described previously, this wind produces enhanced mixing in the near-bed region leading to a decrease in the local density gradient particularly in the shelf-break region (Fig. 8) where as we have shown previously that the nonlinear terms are most important and, hence, any reduction in the density gradient will produce a significant decrease in the amplitude of the higher harmonics. To understand this phenomenon in more detail it is useful to examine the time variations of the σ_t surfaces and the streamfunction over a tidal cycle.

Before considering these changes in the density field, it is of interest to compare contours of turbulence energy and viscosity computed for the downwelling wind condition (Fig. 14) with those computed for the upwelling wind condition (Fig. 11). As discussed previously in connection with the wind-only calculation, the downwelling wind reduces the near-bed density gradient at the top of the shelf and, hence, bed turbulence can penetrate farther into the water column. The same effect is evident in Fig. 14 with a significantly thicker viscous and turbulent boundary layer than found previously (Fig. 11). Also, the additional tidally generated turbulence gives a thicker layer than in the wind-only calculation (cf. Figs. 14 and 9).

From a comparison of σ_t surfaces with wind and tidal forcing at $t = (1/16)T$ (Fig. 15) and the corresponding plot with tidal forcing only (Fig. 5), it is evident that the wind-induced downwelling and the associated mixing has significantly reduced the internal tidal oscillations present in the σ_t surfaces with tidal forcing alone. Also, the streamfunction in the region of the shelf slope shows a smoother spatial variation than that found in the tide-only solution, which shows significant changes in the near-bed region associated with the internal tides propagating along density surfaces.

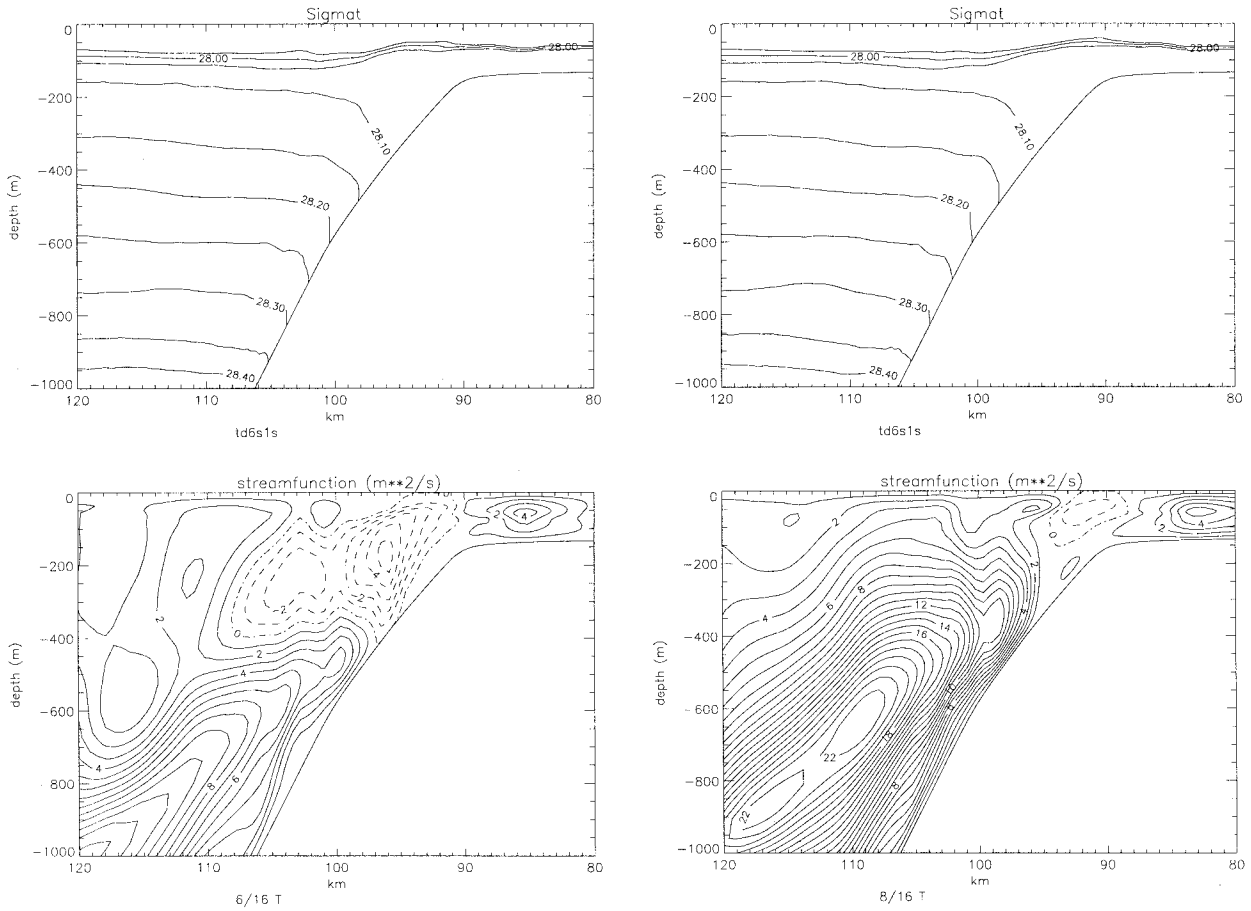

FIG. 15. (*Continued*)

Although the wind-induced downwelling along the shelf slope is maintained, the internal tide produces upwelling and downwelling in this region, which can oppose or enhance the wind-induced downwelling at different locations and times along the shelf slope. At time $t = (3/16)T$ the streamfunction contours show an upwelling along the slope. However, by $t = (5/16)T$ and $t = (6/16)T$ the upwelling associated with the internal tide (Fig. 5) is significantly greater at depth than the downwelling produced by the wind, and the density contours on the shelf slope are moved slightly upward [cf. Fig. 15 at $t = (6/16)T$ and $t = (8/16)T$].

From this comparison it is clear that for the downwelling wind condition there are no significant internal tidal oscillations along density interfaces that intersect the shelf slope. Considering the density surfaces above the shelf slope at a depth of 50 to 100 m, although there is evidence of internal waves along these interfaces, the wavelength is much longer than that found with the tide alone, and there does not appear to be any very short period waves generated in the surface layer above the shelf break of the form found with the tide-only solution. This explains the reduction of the amplitude of the internal displacement at the M_4 frequency and the negligible displacement at the M_6 frequency. This reduction in nonlinear effects is due to the decreased density gradients in the shelf-break region produced by the downwelling wind condition.

b. Calculations using the algebraic eddy viscosity and diffusivity model

In the previous series of calculations, the q^2–q^2l turbulence energy submodel was used to calculate the coefficients for the vertical diffusion of momentum and density. In a recent series of calculations, Xing and Davies (1996e) examined the differences in the internal tide computed using a range of different submodels to determine the various mixing coefficients. No major differences were found in the computed internal tidal displacements and currents determined using a q^2–q^2l model to compute diffusion compared with using an algebraic Richardson number formulation, which is computationally much less expensive. Since this calculation was restricted to the tide only, it is instructive to do a similar comparison with both tidal and wind forcing.

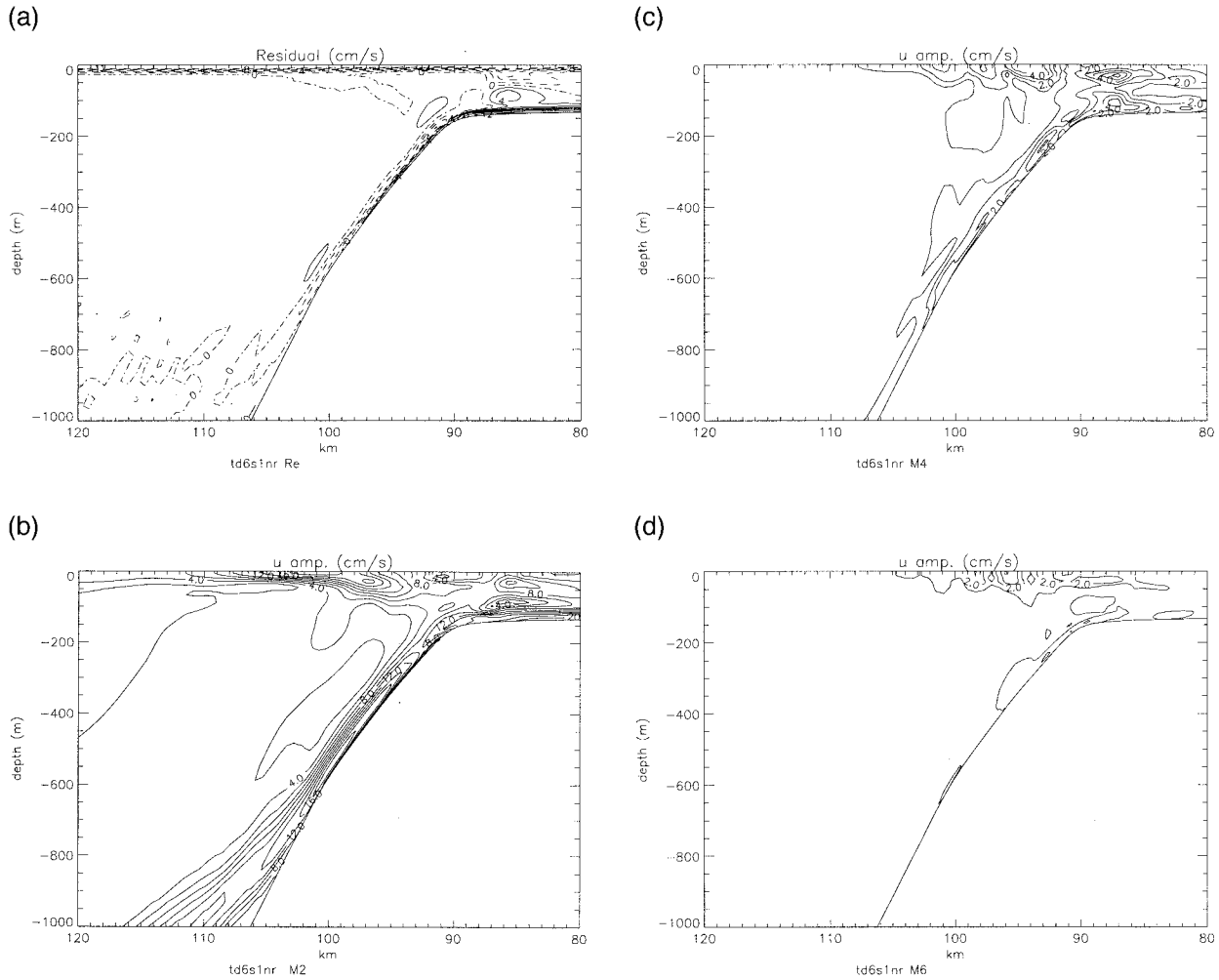

FIG. 16. As in Fig. 10 but with vertical mixing coefficients determined algebraically, as a function of Richardson number. (The internal displacement is not shown.)

1) UPWELLING-FAVORABLE WIND AND TIDAL FORCING (RICHARDSON-NUMBER-DEPENDENT VISCOSITY)

In this calculation (calculation 6, Table 1), the model was forced with both a wind stress of -0.2 N m^{-2} and the tide for an identical period of time to that considered previously. Parameterization of subgrid-scale mixing was accomplished using the algebraic expression, given previously [Eq. (16) and (17)]. By this means it is possible to determine if there are any major differences in the internal currents and displacements due to differences in the submodels used to determine the mixing.

Comparing contours of the residual current due to tide and wind forcing (Fig. 16a) with those computed previously using the q^2–q^2l model (Fig. 10a), it is evident that one significant difference is in the thickness of the surface wind-driven layer, which is larger in the case of the q^2–q^2l model than for the Richardson-number-dependent algebraic eddy viscosity formulation. This is probably because the q^2–q^2l model can take account of an input of wind-induced surface turbulence, which will influence the value of surface eddy viscosity and hence the depth of penetration of the wind's momentum. The surface viscosity will also be influenced in the q^2–q^2l model by the choice of surface roughness length z_s, which is not well known.

Some differences are also evident in the thickness of the bottom boundary layer, with stronger currents confined to the near-bed layer in the model with the Richardson-number-dependent viscosity than with the q^2–q^2l formulation. However, both models show the increase in residual flow above the bottom boundary layer, which occurs on the shelf 85 km from the coast associated with the internal tide.

From a comparison of the amplitude of the u component of the current at the M_2 frequency determined with the algebraic closure model (Fig. 16b) and that computed previously (Fig. 10b), it is clear that both models exhibit similar major features. The region of surface-intensified current (amplitude above 16 cm s^{-1})

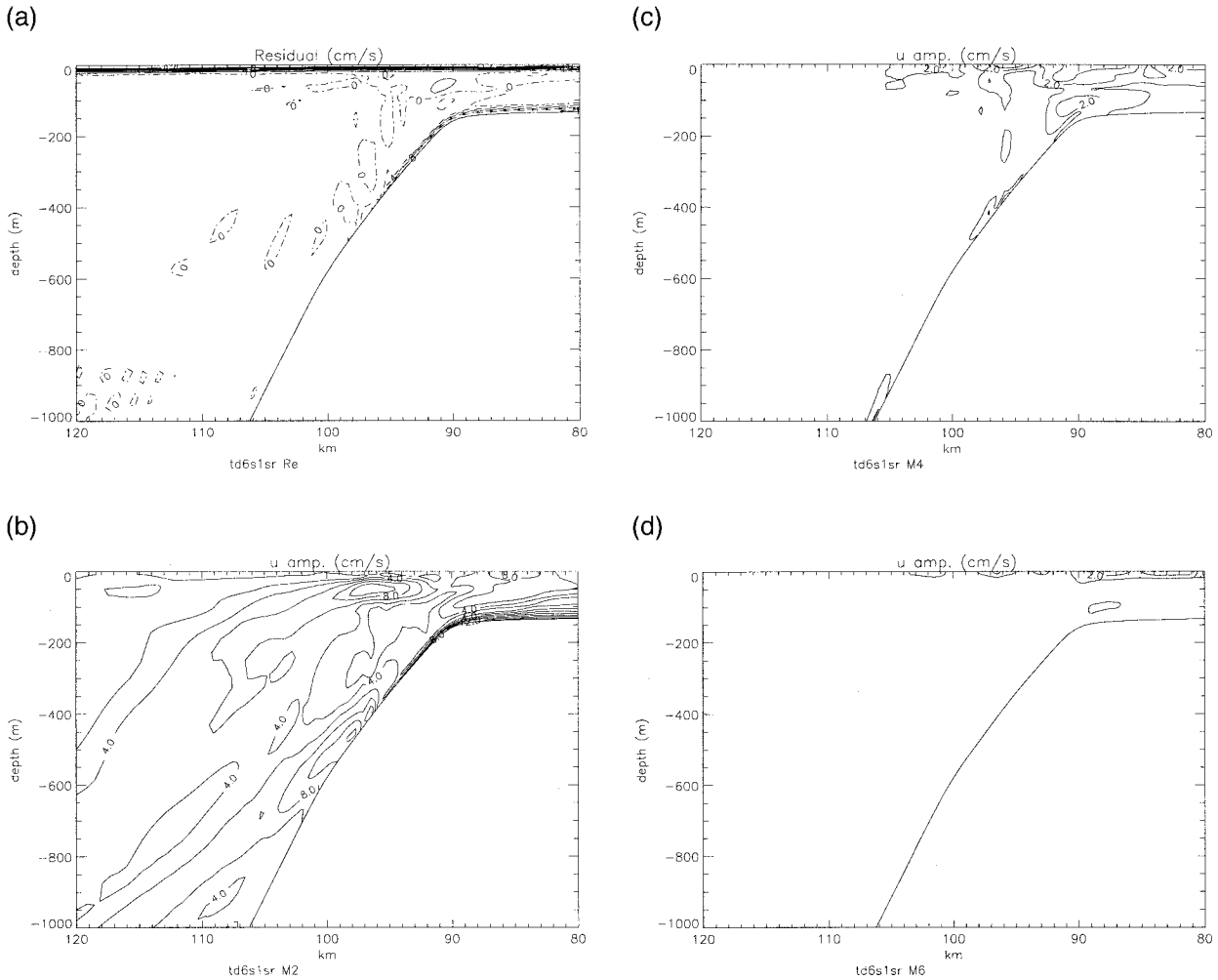

FIG. 17. As in Fig. 16 but with a downwelling wind condition.

that occurs at approximately 98 km offshore in the q^2–q^2l model is also present in the algebraic viscosity model, but now at 102 km offshore. Bottom-intensified currents along the shelf slope at a depth of 600 m are evident in both models, although again the exact location of the position of the maximum is slightly different. These differences can be attributed to the fact that the wind-driven currents, which advect the density fields along the shelf slope, are different in the two models and also that the difference in density diffusion between the two models will contribute to slight differences in the density field, which will influence the location and propagation of the internal tide.

Considering the higher harmonics of the tide, namely, M_4 and M_6 (Figs. 10c,d and 16c,d), again both models show similar spatial features and current intensities with the solution computed using the Richardson number viscosity appearing to be slightly smoother than that determined with the q^2–q^2l model. This result is probably because in the Richardson number formulation, away from the boundary layers, the viscosity and diffusivity cannot fall below the background values given in Eqs. (16) and (17). No such constraint is applied in the q^2–q^2l model where values can fall below 10^{-6} m^2 s^{-1} (Fig. 11).

Although there are slight differences in the flows computed with the two models, the essential features of the effects of the wind upon the internal tide are not significantly different.

2) DOWNWELLING-FAVORABLE WIND AND TIDAL FORCING (RICHARDSON-NUMBER-DEPENDENT VISCOSITY)

In this section we will compare the results of the model using an algebraic eddy viscosity [Eqs. (16) and (17)] with the q^2–q^2l model under conditions of tidal forcing with a downwelling-favorable wind stress of $+0.2$ N m^{-2}. Comparing residual flows (Fig. 17a) with those computed previously with the q^2–q^2l model (Fig. 13a), it is clear that the wind-driven surface and bed layers are much thinner than those found in the q^2–q^2l

model. The reasons for these differences are the same as those discussed previously for the upwelling case.

Comparing the amplitude of the u component of current at the M_2 frequency (Fig. 17b) with that computed previously, it is evident that the subsurface maximum (currents exceeding 8 cm s^{-1}), which occurs at a water depth of about 100 m and at a location 96 km offshore (Fig. 13b), is present in the solution computed with the algebraic viscosity model at a similar location. Similarly, the maximum (currents exceeding 8 cm s^{-1}), which occurs along the shelf slope at a water depth of 500 m, is present in both solutions. The most significant difference between the two models is the existence of a region of strong (currents exceeding 10 cm s^{-1}) near-bed currents on the shelf in the algebraic viscosity model.

From a comparison of the M_4 component of current (Figs. 17c and 13c), it is evident that both models show similar spatial distributions of this component with the region of strongest current (of order 2 cm s^{-1}) occuring at the top of the shelf slope. Again, a spatially more uniform distribution occurs with the Richardson-number-dependent viscosity, for the reasons stated previously.

4. Concluding remarks

The initial sections of this paper have dealt with the formulation of a three-dimensional primitive equation baroclinic model in transport form and its numerical solution using sigma coordinates in the vertical. The calculation of the vertical diffusion of momentum and density was accomplished using either a two-equation turbulence energy model or an algebraic expression depending upon Richardson number. Horizontal diffusion was parameterized using either a Laplacian or biharmonic form of the diffusion with a constant coefficient.

The model was applied in cross-sectional form to the calculation of the internal tidally generated currents and displacements and also the currents and displacements produced by upwelling and downwelling wind stress conditions of magnitude 0.2 N m^{-2}. A horizontal grid resolution of order 0.6 km with 50 sigma levels in the vertical was used in these calculations. No significant differences in results computed using Laplacian or biharmonic friction were found, suggesting that with the fine grid and low horizontal diffusion coefficients used here the solution was insensitive to the exact form of horizontal diffusion, and the Laplacian was used in all subsequent calculations.

Tidal calculations showed that besides the generation of the internal tide, short internal waves were produced in the region above the shelf slope due to the nonlinear terms in the equations. The production of strong internal tidal currents at the top of the shelf break lead to increased mixing in the surface and bed layers in this region.

Calculations with upwelling and downwelling wind conditions showed that, in the case of upwelling, the density gradient in the near-bed region was increased and the bottom turbulent boundary layer thickness was much thinner than in the downwelling case. Calculations with downwelling wind conditions showed that as lighter water was forced below heavier water, intensified mixing took place leading to an increased thickness of the bottom boundary layer, and increased near-bed turbulence. The results of these numerical calculations exhibited the main features of the idealized analytical solutions of MacCready and Rhines (1993).

Calculations with both tidal forcing and upwelling-favorable winds showed that the major features of the M_2 component of the internal tide were similar to those found with the tide alone, although there are some enhancements in the higher harmonics of the tide due to the wind-induced increase in the near-bed density gradients at the top of the shelf slope. Turbulence energy and viscosity in the surface and bed layers showed increased intensity above that found with the tide only due to the increased mixing produced by the wind. In the case of tidal forcing and a downwelling wind condition, the magnitude of the M_2 component of the tide and its higher harmonics was significantly reduced due to the decrease in the density gradient in the region of internal tide production. The decrease in the density gradient in the upper part of the shelf slope decreased the buoyancy supression of turbulence and gave a much thicker turbulent bottom boundary layer there.

The major features of the changes in the magnitude of the internal tide due to upwelling and downwelling wind conditions were also reproduced by the model using a simple algebraic expression for the mixing as a function of the Richardson number. Although this model can reproduce the major changes, it did not give any insight into the spatial variation of the turbulence energy. With the development of measuring methods capable of determining turbulence energy dissipation rates (e.g., Gargett 1994) and the acquisition of such datasets in shallow seas (e.g., Simpson et al. 1996) and in shelf break regions (Sandstrom and Oakey 1995), there exists the possibility of validating the more complex models against direct turbulence measurements rather than against field data such as currents and displacements that do not appear to be particularly sensitive to the form of the turbulence model. However, from calculations of Xing and Davies (1996e) it is evident that to rigorously validate the q^2–q^2l type model requires, besides turbulence energy dissipation datasets, the accurate measurement of both bottom topography and the internal density field. From the results presented here it is evident that the magnitude of the internal tide off the west of Scotland can be reduced by a downwelling-favorable wind, although this gives rise to a thicker turbulent bottom boundary layer in which measurements can be made. However, the separation of tidal turbulence from modifications in total

turbulence due to tide and wind in the near-bed region may be very difficult in any field experiment.

Acknowledgments. The authors are indebted to Robert Smith for help in preparing diagrams and Jean Smith, Linda Parry, and Linda Ravera for typing the paper.

REFERENCES

Baines, P. G., 1982: On internal tide generation models. *Deep-Sea Res.*, **29,** 307–338.

Baumert, H., and G. Radach, 1992: Hysteresis of turbulent kinetic energy in nonrotational tidal flows: A model study. *J. Geophys. Res.*, **97,** 3669–3677.

Blumberg, A. F., and G. L. Mellor, 1987: A description of a three-dimensional coastal ocean circulation model. *Three-Dimensional Coastal Ocean Models*, N. S. Heaps, Ed., Amer. Geophys. Union, 1–16. (Coastal and Estuarine Sciences, No. 4).

Chuang, W.-S., and D.-P. Wang, 1981: Effects of density front on the generation and propagation of internal tides. *J. Phys. Oceanogr.*, **11,** 1357–1374.

Craig, P. D., 1987: Solutions for internal tidal generation over coastal topography. *J. Mar. Res.*, **45,** 83–105.

Davies, A. M., and J. E. Jones, 1990: Application of a three-dimensional turbulence energy model to the determination of tidal currents on the northwest European shelf. *J. Geophys. Res.*, **95,** 18 143–18 162.

——, and ——, 1991: On the numerical solution of the turbulence energy equations for wave and tidal flows. *Int. J. Numer. Methods Fluids*, **12,** 17–41.

——, and H. Gerritsen, 1994: An intercomparison of three dimensional tidal hydrodynamic models of the Irish Sea. *Tellus*, **46A** (2), 200–221.

——, and J. Lawrence, 1994: Examining the influence of wind and wind wave turbulence on tidal currents, using a three-dimensional hydrodynamic model including wave-current interaction. *J. Phys. Oceanogr.*, **24,** 2441–2460.

——, and ——, 1995: Modeling the effect of wave-current interaction on the three-dimensional wind-driven circulation of the eastern Irish Sea. *J. Phys. Oceanogr.*, **25,** 29–45.

——, and J. Xing, 1995: An intercomparison and validation of a range of turbulence energy schemes used in three dimensional tidal models. *Qualitative Skill Assessment for Coastal Ocean Models*, D. R. Lynch, and A. M., Davies, Eds., AGU Coastal and Estuarine Series, Amer. Geophys. Union, 71–95.

Ellett, D. J., A. Edwards, and R. Bowers, 1986: The hydrography of the Rockall Channel—An overview. *The Oceanography of the Rockall Channel Proceedings of the Royal Society of Edinburgh 88B*, 61–81.

Galperin, B., L. H. Kantha, S. Hassid, and A. Rosati, 1988: A quasi-equilibrium turbulent energy model for geophysical flows. *J. Atmos. Sci.*, **45,** 55–62.

——, A. Rosati, L. H. Kantha, and G. L. Mellor, 1989: Modeling rotating stratified turbulent flows with application to oceanic mixed layers. *J. Phys. Oceanogr.*, **19,** 901–916.

Gargett, A. E., 1994: Observing turbulence with a modified acoustic doppler current profiler. *J. Atmos. Oceanic Technol.*, **11,** 1592–1610.

Gaspar, P., Y. Gregoris, and J.-M. Lefeure, 1990: A simple eddy kinetic energy model for simulations of the oceanic vertical mixing: Tests at station Papa and long-term upper ocean study site. *J. Geophys. Res.*, **95,** 16 179–16 193.

Heathershaw, A. D., A. L. New, and P. D. Edwards, 1987: Internal tides and sediment transport at the shelf break in the Celtic Sea. *Contin. Shelf Res.*, **7,** 485–517.

——, J. Small, and C. E. Stretch, 1994: Frictional formulations in numerical ocean models and their effect on simulated acoustic fields. *J. Phys. Oceanogr.*, **24,** 274–297.

Holloway, P. E., 1984: On the semi-diurnal internal tide at a shelf-break region on the Australian north-west shelf. *J. Phys. Oceanogr.*, **14,** 1778–1790.

——, 1996: A numerical model of internal tides with application to the Australian North West Shelf. *J. Phys. Oceanogr.*, **26,** 21–37.

James, I. D., 1996: Advection schemes for shelf sea models. *J. Mar. Syst.*, **8,** 237–254.

Johns, B., and T. Oguz, 1987: Turbulent energy closure schemes. *Three-Dimensional Coastal Ocean Models*, N. S. Heaps, Ed., Amer. Geophys. Union, 17–40.

Lamb, K. G., 1994: Numerical experiments of internal wave generation by strong tidal flow across a finite amplitude bank edge. *J. Geophys. Res.*, **99,** 843–864.

Luyten, P. J., 1996: An analytical and numerical study of surface and bottom boundary layers with variable forcing and application to the North Sea. *J. Mar. Syst.*, **8,** 171–190.

——, E. L. Deleersnijder, J. Ozer, and K. G. Ruddick, 1996: Presentation of a family of turbulence closure models for stratified shallow water flows and preliminary application to the Rhine outflow region. *Contin. Shelf Res.*, **16,** 101–130.

MacCready, P., and P. B. Rhines, 1993: Slippery bottom boundary layers on a slope. *J. Phys. Oceanogr.*, **23,** 5–22.

Martinsen, E. A., and H. Engedahl, 1987: Implementation and testing of a lateral boundary scheme as an open boundary condition in a barotropic ocean model. *Coastal Eng.*, **11,** 603–627.

Munk, W. H., and E. R. Anderson, 1948: Notes on a theory of the thermocline. *J. Mar. Res.*, **7,** 276–295.

New, A. L., 1988: Internal tidal mixing in the Bay of Biscay. *Deep-Sea Res.*, **35,** 691–709.

——, and R. D. Pingree, 1990: Evidence for internal tidal mixing near the shelf break in the Bay of Biscay. *Deep-Sea Res.*, **37,** 1783–1803.

Oey, L.-Y., and P. Chen, 1992a: A nested-grid ocean model: With application for the simulation of meanders and eddies in the Norwegian coastal current. *J. Geophys. Res.*, **97,** 20 063–20 086.

——, and ——, 1992b: A model simulation of circulation in the northeast Atlantic shelves and seas. *J. Geophys. Res.*, **97,** 20 087–20 115.

Proctor, R., and J. Wolf, 1990: An investigation of the Storm Surge of February 1, 1983 using numerical models. *Modeling Marine Systems*, Vol. 1, A. M. Davies, Ed., CRC Press, 43–72.

——, and A. M. Davies, 1996: A three dimensional model of tides off the north-west coast of Scotland. *J. Mar. Syst.*, **7,** 43–66.

Sandstrom, H., and N. S. Oakey, 1995: Dissipation in internal tides and solitary waves. *J. Phys. Oceanogr.*, **25,** 604–614.

Sherwin, T. J., 1988: Analysis of an internal tide observed on the Malin Shelf, north of Ireland. *J. Phys. Oceanogr.*, **18,** 1035–1050.

——, 1991: Evidence of a deep internal tide in the Faeroe–Shetland Channel. *Tidal Hydrodynamics*, B. B. Parker, Ed., John Wiley and Sons, 469–488.

——, and N. K. Taylor, 1989: The application of a finite difference model of internal tide generation to the NW European Shelf. *Dtsch. Hydrogr. Z.*, **42,** 151–167.

——, and ——, 1990: Numerical investigations of linear internal tide generation in the Rockall Trough. *Deep-Sea Res.*, **37,** 1595–1618.

Signell, R. P., R. C. Beardsley, H. C. Graber, and A. Capotondi, 1990: Effect of wave–current interaction on wind-driven circulation in narrow, shallow embayments. *J. Geophys. Res.*, **95,** 9671–9678.

Simpson, J. H., W. Crawford, T. P. Rippeth, A. R. Campbell, and J. V. S. Cheok, 1996: The vertical structure of turbulent dissipation in shelf seas. *J. Phys. Oceanogr.*, **26,** 1579–1590.

Xing, J., and A. M. Davies, 1996a: Application of turbulence energy

models to the computation of tidal currents and mixing intensities in shelf edge regions. *J. Phys. Oceanogr.*, **26,** 417–447.

——, and ——, 1996b: The influence of mixing length formulation and stratification upon tidal currents in shallow seas. *Estuar. Coastal Shelf Sci.*, **42,** 417–456.

——, and ——, 1996c: Application of a range of turbulence energy models to the determination of M_4 tidal current profiles. *Contin. Shelf Res.*, **16,** 517–547.

——, and ——, 1996d: Formulation of a three-dimensional shelf edge model and its application to internal tide generation. *Contin. Shelf Res.*, in press.

——, and ——, 1996e: Application of a range of turbulence energy models to the computation of the internal tide. *Int. J. Numer. Methods Fluids*, in press.

——, and ——, 1996f; Processes influencing the internal tide, its higher harmonics and tidally induced mixing on the Malin–Hebrides shelf. *Progress in Oceanography*, Vol. 38, Pergamon, 155–204.